Physics of Fluids

RESEARCH ARTICLE | OCTOBER 06 2022

Effect of expansion on the wall heat flux in a supersonic turbulent boundary layer

Fulin Tong (童福林); Siwei Dong (董思卫); Junyi Duan (段俊亦); ... et. al

Check for updates

Physics of Fluids 34, 105109 (2022)
https://doi.org/10.1063/5.0113514

CrossMark

View Online

Export Citation

Articles You May Be Interested In

Wall shear stress and wall heat flux in a supersonic turbulent boundary layer

Physics of Fluids (January 2022)

Wall heat flux in a supersonic shock wave/turbulent boundary layer interaction

Physics of Fluids (June 2022)

Enhancement of flame retardancy and mechanical properties of poly(butylene succinate) composites by adding hybrid fillers

AIP Conference Proceedings (October 2020)

Downloaded from http://pubs.aip.org/aip/pof/article-pdf/doi/10.1063/5.0113514/16584511/105109_1_online.pdf

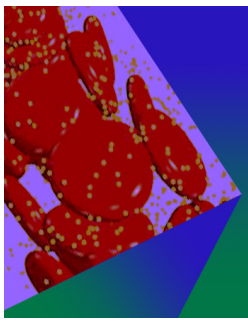

Physics of Fluids

Special Topic: Flow and Forensics

Submit Today!

AIP Publishing

AIP Publishing

Physics of Fluids ARTICLE scitation.org/journal/phf

Effect of expansion on the wall heat flux in a supersonic turbulent boundary layer

Cite as: Phys. Fluids **34**, 105109 (2022); doi: 10.1063/5.0113514
Submitted: 23 July 2022 · Accepted: 10 September 2022 ·
Published Online: 6 October 2022

View Online Export Citation CrossMark

Fulin Tong (童福林),[1] Siwei Dong (董思卫),[1] Junyi Duan (段俊亦),[2,3] Xianxu Yuan (袁先旭),[1,a)] and Xinliang Li (李新亮)[2,3]

AFFILIATIONS

[1]State Key Laboratory of Aerodynamics, 621000 Mianyang, China
[2]LHD, Institute of Mechanics, Chinese Academy of Sciences, 100190 Beijing, China
[3]School of Engineering Science, University of Chinese Academy of Sciences, 100049 Beijing, China

[a)]Author to whom correspondence should be addressed: yuanxianxu@cardc.cn

ABSTRACT

Direct numerical simulation of a spatially developing supersonic turbulent boundary layer at a Mach number of 2.25 and a friction Reynolds number of $Re_\tau = 769$ subjected to an expansion corner with a deflection angle of 12° is performed to investigate the effect of expansion on the characteristics of the wall heat flux (WHF). The effect of expansion on the statistical and structural properties of the fluctuating WHF is analyzed systematically in terms of probability density function, frequency spectra, and space-time correlations. Normalization using the local root mean square value yields good collapse of the probability density function curves. Unlike with wall pressure frequency spectra, it is found that expansion has little influence on the low-frequency components of the WHF spectrum. The correlation results show that the main effect of expansion is to increase the characteristic length scales and convection velocity of the WHF fluctuation in the post-expansion region. Furthermore, a direct comparison between the conditionally averaged flow fields and those presented in the authors' previous work [Tong *et al.*, Phys. Fluids **34**, 015127 (2022)] is performed to uncover the effect of expansion on the flow structures associated with extreme positive and negative WHF fluctuation events. We highlight that the extreme positive event emerges below a small hot spot under the action of a strong Q4 event, whereas the extreme negative event is relatively insensitive to expansion and still occurs between a pair of strong oblique vortices. In addition, we decompose the mean WHF into seven physics-informed contributions and quantify the effect of expansion on the dominating components with the aid of the bidimensional empirical mode decomposition method. The scale-decomposed results demonstrate quantitatively that expansion decreases the contribution of the large-scale structures in the outer region but the small-scale structures in the near-wall region contribute heavily to the mean WHF generation in the downstream region.

Published under an exclusive license by AIP Publishing. https://doi.org/10.1063/5.0113514

I. INTRODUCTION

The expansion corner is of fundamental interest in the context of wall-bounded flows under favorable pressure gradients. When a compressible turbulent boundary layer passes through an expansion corner, its density decreases rapidly and the accelerated boundary layer is subject to the combined effects of favorable streamwise pressure gradient, convex streamline curvature, and bulk dilatation, as noted by Bradshaw.[1] It is well accepted that turbulence downstream of the expansion is suppressed greatly and the boundary layer is stabilized. If the expansion is strong enough (large deflection angle), the distorted boundary layer experiences relaminarization in the relaxation region, as documented by Sreenivasan[2] and Bourassa and Thomas.[3] Although significant advances have been made over the past few decades, the effect of expansion on wall-flow variables is not yet fully understood. This is especially true for wall heat flux (WHF). A better understanding of its relaxation in the expansion region would aid novel thermal protection system and scramjet engine inlet designs.

The effect of expansion on turbulence intensities has commonly been studied in compressible boundary layers over expansion corners. Previous experiments and numerical simulations have demonstrated that bulk dilatation, which acts as the primary stabilizer, is mainly responsible for reduction of the turbulence intensity. This reduction is large in the distorted boundary layer and increases with the Mach number, as noted by Spina *et al.*[4] For example, Dussauge and Gaviglio[5] used direct comparisons between experimental measurements and rapid distortion theory calculations to investigate the effect of bulk dilatation on turbulent fluctuations in a turbulent boundary layer at Mach 1.76 over a 12° centered expansion corner. They found

Downloaded from http://pubs.aip.org/aip/pof/article-pdf/doi/10.1063/5.0113514/16584511/105109_1_online.pdf

Published under an exclusive license by AIP Publishing

that the theoretical analysis, which only considered dilatation effects, reproduced the reduction in the longitudinal turbulence intensity in the outer part of the disturbed boundary layer well. Later, the rapid distortion approximation proposed by Dussauge and Gaviglio[5] was further supported by Smith and Smits[6] via an experiment that identified a stronger distortion using a Mach 2.84 turbulent boundary layer in a 20° centered expansion corner. They highlighted an encouraging agreement between the computed and measured Reynolds stresses. This confirmed the large influence of bulk dilation on the decrease in the Reynolds stress. Using laser Doppler velocimetry in a Mach 3 turbulent boundary layer ($Re_\theta = 40\,000$) developing along a centered expansion corner with a deflection angle of 14°, Arnette *et al.*[7] observed that the turbulent kinetic energy levels decreased sharply and that the sign of the Reynolds shear stress changed. This implied an apparent reverse transition downstream of the expansion. The dominance of bulk dilatation during turbulence reduction was examined analytically via analysis of the compressible vorticity transport equation. The results were consistent with the perturbation impulse estimates proposed by Spina *et al.*[4] Furthermore, the experiment performed by Dussauge and Gaviglio[5] was studied numerically again by Nguyen *et al.*,[8] Konopka *et al.*,[9] and Teramoto *et al.*,[10] who analyzed the turbulent kinetic energy transport equation and the anisotropy of the Reynolds stress tensor. They revealed that the near-wall turbulence in the expanding flow attained the one-component limit and the negative production of turbulent kinetic energy was caused by bulk dilatation in the expansion fan.

The effect of expansion on the behaviors of turbulent structures is another important issue considered in many studies of compressible turbulent expansion flows. Arnette *et al.*[11] performed experiments in four expansion regions that corresponded to centered and gradual 7° and 14° expansions at Mach 3. They showed that the small-scale structures in the near-wall region and large-scale structures in the outer region exhibit apparently different motions during expansion and observed a more intermittent boundary layer downstream of the expansion. Their filtered Rayleigh scattering visualizations suggested that, in response to bulk dilatation, the small-scale structures were quenched rapidly after the initial expansion. In contrast, large-scale structures in the outer part survived the expansion, after which their scale increases but the magnitude of their density decreases. Recently, Humble *et al.*[12] performed experiments at Mach 4.9 to investigate the responses of inner small-scale and outer large-scale structures to convex curvature. They proposed an idealized conceptual model to account for coherent motions within the initial expansion region and used fractal theory to explain the effect of bulk dilatation on quenching of the small-scale structures.

Recently, Fang *et al.*[13] studied the Mach 2.9 turbulent boundary layer over a tandem expansion-compression corner configuration numerically by using direct numerical simulation (DNS) to uncover the flow structure evolution in the expansion region. A characteristic two-layer structure, similar to the finding in the experiments by Arnette *et al.*,[11] was observed. In addition, the different turbulence evolution characteristics within the inner and outer layers were confirmed. However, the researchers found that suppression of turbulence in the inner layer occurred only in a small region after the expansion and the inner turbulence was amplified significantly in the other regions due to the shock wave interaction. Furthermore, Sun *et al.*[14] performed DNS studies of expansion corners with deflection angles of 2° and 4° at Mach 2.7. They focused on the effect of expansion on turbulence structure recovery and found that turbulence recovered to the equilibrium state more quickly in the inner layer than in the outer layer. The turbulent kinetic energy profiles and budgets revealed a two-layer structure in the recovery region. As explained by Sun *et al.*,[14] the quick recovery in the near-wall region and the slow recovery in the outer region were closely related to the outer turbulence decay history effects, which limited momentum and energy exchanges between the two layers.

Regarding the effect of expansion on surface quantities, considerable experimental studies have been aimed at the wall pressure. Using mean wall pressure distributions, Lu and Chung[15] proposed a scaling law for the downstream influence of the expansion and validated that the downstream influence was characterized primarily by an inviscid parameter $K = M_\infty \alpha$, where α is the deflection angle (in radians) of the corner. In a follow-up work, Chung[16] experimentally validated the downstream influence scaling in a lower supersonic expansion corner flow. The increased corner deflection angle changed the downstream influence little. It was suggested that the scaling law might be only applicable to high Mach flows. Wall pressure fluctuations in Mach 8 flows past small expansion corners were investigated by Chung and Lu,[17] who stated that the expansion process severely attenuated the normal fluctuation distribution and observed that the fluctuating wall pressure was not recovered completely within $4–6\delta_0$ (where δ_0 is the boundary layer thickness upstream of the corner), which was much slower than that for the mean pressure. Dawson *et al.*[18] performed an experimental campaign that studied centered and gradual expansions to characterize the influence of varying degrees and expansion rates on wall pressure fluctuation spectra. Multipoint wall pressure measurements were used. The power spectrum distributions measured just downstream of the corners shifted to lower frequencies and exhibited a decrease in high frequencies. This matched a footprint of quenched small-scale structures in the near wall region. However, there are a few studies of WHF in compressible expansion flows. Bloy[19] measured the mean wall pressure and WHF for the expansion of a hypersonic turbulent boundary layer at a sharp corner. The WHF downstream of the corner was compared to local flat-plate boundary-layer similarity theory solutions. To our knowledge, there is no available data regarding wall heat flux fluctuations in the published literature and little is known regarding the behavior of the fluctuating WHF during expansion.

The main purpose of the present study is to address the limitations of the literature by documenting the effect of expansion on the mean and fluctuating WHFs via DNS. In our prior work,[20] the flow associated with extreme events and the scale-based decomposition of WHF in a Mach 2.25 fully developed turbulent boundary layer was analyzed. In this paper, we extend this previous study and investigate the characteristics of WHF in a Mach 2.25 turbulent boundary layer over a 12° centered expansion corner. A cold wall thermal condition is used with a wall-to-recovery-temperature ratio of 0.75. The parameter proposed by Narasimha and Viswanath[21] is $\Delta p/\tau_o = 113$, where Δp is the pressure drop during the expansion process and τ_o is the wall shear stress upstream of the expansion corner. Thus, the relaminarization is expected downstream of the expansion. In the present study, we focus on the global fluctuating WHF fields in the expansion region, which are difficult to measure, and highlight the effect of expansion on quantitative contributions of turbulent structures to mean WHF generation

Downloaded from http://pubs.aip.org/aip/pof/article-pdf/doi/10.1063/5.0113514/16584511/105109_1_online.pdf

Published under an exclusive license by AIP Publishing

using bidimensional empirical mode decomposition (BEMD) introduced by Koll *et al.*[22] The remainder of this paper is structured as follows. Section II introduces the details of the DNS, including the numerical method, computational set-up, grid, and numerical validity. In Sec. III, the statistical properties and conditional analysis of the fluctuating WHF and scale-based decomposition of the mean WHF are presented. Finally, conclusions are presented in Sec. IV.

II. DIRECT NUMERICAL SIMULATION

A. Numerical methodology and inflow conditions

An open-source, high-order, finite difference flow solver, Opencfd-SC, is used in our simulation. This solver has been applied successfully to a wide body of studies on supersonic and hypersonic flows such as transition over a blunt cone[23] and shock wave/boundary layer interactions.[24–26] The flow is governed by the three-dimensional compressible unsteady Navier–Stokes equations in their conservative forms, which are solved using curvilinear coordinates. The inflow parameters are used to non-dimensionalize the governing equations and a perfect gas with a specific heat capacity ratio $\gamma = 1.4$ is taken as the working fluid. The viscosity coefficient μ and thermal conductivity k are calculated using Sutherland's law and $k = \mu C_p/Pr$, respectively. The specific heat capacity of the gas at a constant pressure C_p and the molecular Prandtl number Pr are taken as $C_p = \gamma R/(\gamma - 1)$ and $Pr = 0.71$, respectively, where R denotes the specific gas constant. The thermodynamic variables are governed by the ideal gas state equation. The strain-rate tensor S_{ij} and the viscous stress tensor σ_{ij} are assumed to obey the constitutive relation for a Newtonian fluid. The heat flux vector q_j is obtained from Fourier's law of heat condition. The details of the governing equations are given in Tong *et al.*[25]

This code directly solves the governing equations and no modeling is used. The inviscid fluxes are discretized using a fourth-order weighted essentially non-oscillatory (WENO) scheme with relative and absolute limiters,[27,28] in which a symmetric collection of candidate stencils is applied and the weights in the linear part of the original WENO[29] are optimized. This scheme is low dissipative and robust to compressible flows with strong discontinuities, which has been validated extensively in many DNS studies. A detailed description of the optimized weights and limiters can be found in Wu and Martin[27] and Martin *et al.*[28] For the viscous fluxes, discretization is performed via a standard eighth-order central difference scheme. A third-order total variation diminishing Runge–Kutta method proposed by Gottlieb and Shu[30] is used for the time integration.

The free-stream inflow parameters are selected in accordance with the M2.25 DNS studies of Tong *et al.*[20,31] for a zero-pressure-gradient flat plate and a reflected interaction. The free-stream Mach number is $M_\infty = 2.25$, the free-stream static temperature is $T_\infty = 169.44$ K, and the unit free-stream Reynolds number is $Re_\infty/\text{mm} = 2.5 \times 10^4$. The inflow turbulent boundary layer is generated via the laminar-to-turbulent transition method, as previously used by Pirozzoli *et al.*,[32] where an inflow laminar boundary layer is triggered and evolves spatially to a fully developed turbulence state. The inflow laminar boundary layer is generated via an auxiliary laminar computation with the same inflow conditions and the inflow boundary layer thickness is $\delta_{in} = 0.508$ mm. The transition is induced by unsteady velocity disturbances in the wall blowing and suction region, which is set downstream of the inflow boundary layer. The disturbances are generated by two temporal modes, two spatial modes in the streamwise direction, and ten spatial modes in the spanwise direction. Thus, a zero net flow rate was obtained at the wall. Detailed expressions for the disturbances are given in Fang *et al.*[33] In addition, the disturbance amplitude and fundamental frequency used in the present study are identical to those of Tong *et al.*[20,31] Throughout this paper, the subscripts "∞" refer to quantities in the free-stream flow.

B. Computational domain and simulation set-up

The computational domain for the DNS of the 12° expansion corner is illustrated in Fig. 1, where the coordinate systems are also presented. Lowercase x, y, and z denote the streamwise direction along the bottom wall, wall-normal direction, and spanwise direction, respectively, whereas uppercase X, Y, and Z denote the corresponding directions in Cartesian coordinates. Throughout this paper, the velocity components in (x, y, z) are denoted by u, v, and w, respectively. The flow variables U, V, and W represent the velocity components in the X, Y, and Z directions, respectively. The size of the domain in the x direction is $L_x = 185.4\delta_{in}$. The tip of the corner x_o is located at $x = 0$ and the domain inlet is located at $x = -142.3\delta_{in}$. Thus, the lengths of the upstream flat-plate and the expansion corner are $L_i = 142.3\delta_{in}$ and $L_c = 43.1\delta_{in}$, respectively. It was found by Tong *et al.*[20] that a fully developed turbulent boundary layer was generated after $x > 125\delta_{in}$. In the present study, we chose a streamwise distance of $142.3\delta_{in}$ before the expansion corner, which is long enough to generate a realistic turbulent inflow upstream of the expansion. The blowing and suction region at the wall extends from $x_a = -127.4\delta_{in}$ to $x_b = -102.4\delta_{in}$. The domain sizes in the y and z directions are $L_y = 17.5\delta_{in}$ and $L_z = 8.7\delta_{in}$, respectively.

We discretize the domain using a mesh consisting of $n_x \times n_y \times n_z = 3042 \times 430 \times 340$ grid points, where the grid is distributed equally in the z direction. Figure 2 shows a sketch of the grid distribution in the x–y plane. In the x direction, the transition zone ($-142.3\delta_{in} < x < -42.3\delta_{in}$) contains a total of 400 points, which are refined progressively. A total of 2632 points are spaced uniformly in the well-resolved zone that extends from $x = -42.3\delta_{in}$ to $x = 35.3\delta_{in}$, where

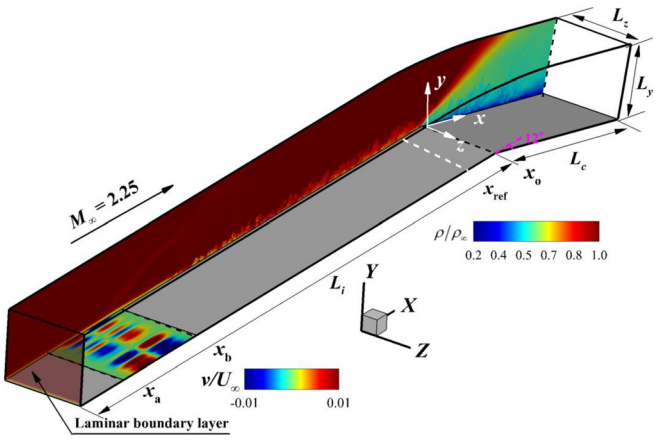

FIG. 1. A sketch of the computational domain. The flow configuration is illustrated using the contour of the density ρ/ρ_∞ in the x–y plane at $z = 0$. The wall blowing and suction region is highlighted by the contour of the wall-normal velocity v between x_a and x_b. x_{ref} denotes the reference station and the tip of the corner is denoted by x_o.

Downloaded from http://pubs.aip.org/aip/pof/article-pdf/doi/10.1063/5.0113514/16584511/105109_1_online.pdf

Published under an exclusive license by AIP Publishing

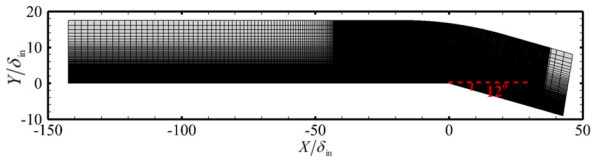

FIG. 2. A sketch of the computational mesh in the x–y plane with every five points in the x direction and every three points in the y direction shown.

the turbulent boundary layer experiences a 12° expansion. The grid in the fringe zone at $x > 35.3\delta_{in}$ is coarsened sharply and includes only 10 points. In the y direction, the grid is clustered toward the wall to resolve the turbulent fluctuations inside the boundary layer. There are about 280 points located between the wall and $y/\delta_{in} = 2.8$. In wall units at $x_{ref} = -17.4\delta_{in}$ (located in the upstream turbulent boundary layer, see Fig. 1), the streamwise spacing in the well-resolved zone is $\Delta x^+ = 8.5$. The spanwise spacing is $\Delta z^+ = 7.15$ and the wall-normal spacing gradually increases from $\Delta y^+ = 0.55$ at the first grid point above the wall to $\Delta y^+ = 5.5$ at $y/\delta_{in} = 2.8$. The grid resolutions in the present study compare well with previous DNS studies of compressible turbulent boundary layers by Sun *et al.*[14,34] and Wang *et al.*[35] The superscript "+" indicates that a quantity is scaled in wall units at x_{ref}, and the subscript "w" denotes condition at the wall, hereafter.

A steady laminar boundary layer profile, given by Tong *et al.*,[20] is applied at the domain inlet. Supersonic outflow boundary conditions are enforced at the domain outlet. The sharply coarsened grid used in the fringe region, as suggested by Pirozzoli *et al.*,[32] drives the flow to a uniform state. At the upper boundary, disturbance reflections back into the domain are inhibited by using a nonreflecting boundary condition. At the bottom wall, a no-slip isothermal boundary condition is enforced and a cold-wall condition is used, where the temperature is fixed to $T_w = 254.16$ K (about 0.75 times the recovery temperature T_r). Unsteady wall-normal velocity disturbances are enforced between x_a and x_b. As suggested by Tong *et al.*,[20,31] the amplitude and basic frequency are chosen as $A = 0.15U_\infty$ and $\varpi = 0.157\, U_\infty/\delta_{in}$, respectively, to accelerate the transition process. Spanwise homogeneity of the flow is ensured by the large spanwise width used in the present study, and then periodic boundary conditions are applied in the z direction. The calculation is started by initializing a three-dimensional flow field, in which the inflow laminar boundary layer profile is used, and is advanced for a period of $380\delta_{in}/U_\infty$ (or two flow-through periods) to wash out the effect of the initial transient flow. The simulation is continued for a period of $990\delta_{in}/U_\infty$ (or five flow-through periods) to perform sample collection after the flow attains statistical steadiness. The statistical convergence of the flow properties is guaranteed by averaging 300 three-dimensional flow fields in the time and the spanwise directions, which are sampled at time intervals of $3.3\delta_{in}/U_\infty$. Throughout this paper, the Reynolds and density-weighted averages for a generic variable f are defined as $\bar{f}$ and $\tilde{f} = \overline{\rho f}/\bar{\rho}$, respectively, with the corresponding fluctuations being $f' = f - \bar{f}$ and $f'' = f - \tilde{f}$. To estimate frequency spectra and space-time correlations of the fluctuating WHF fields accurately, a constant small time interval of $0.05\delta_{in}/U_\infty$ is used to collect the full time-resolved signals in the x–z plane at the wall. The BEMD analysis in the WHF decomposition is performed using 3700 flow samples in the y–z plane. These samples are collected at time intervals of $0.25\delta_{in}/U_\infty$.

C. Grid and numerical validity

We first assess the effect of the selected spanwise width on the DNS results. The spanwise two-point correlation coefficients $R_{\alpha\alpha}$ of the velocity fluctuations, defined by Pirozzoli *et al.*,[32] are given in Fig. 3, where the computed correlation results at four wall-normal locations $y^+ = 20$, 45, 188, and 478 with $x = 0.2\delta_{in}$ (just after the point of the corner) are displayed as functions of the spanwise distance r_z. Clearly, a rapidly decaying correlation coefficient can be seen at larger spanwise distances. All of the coefficients in the inner and outer regions approach zero over a spanwise distance of $L_z/2$. This indicates that the domain width used in the present study is reasonable and can provide reliable turbulence dynamics.

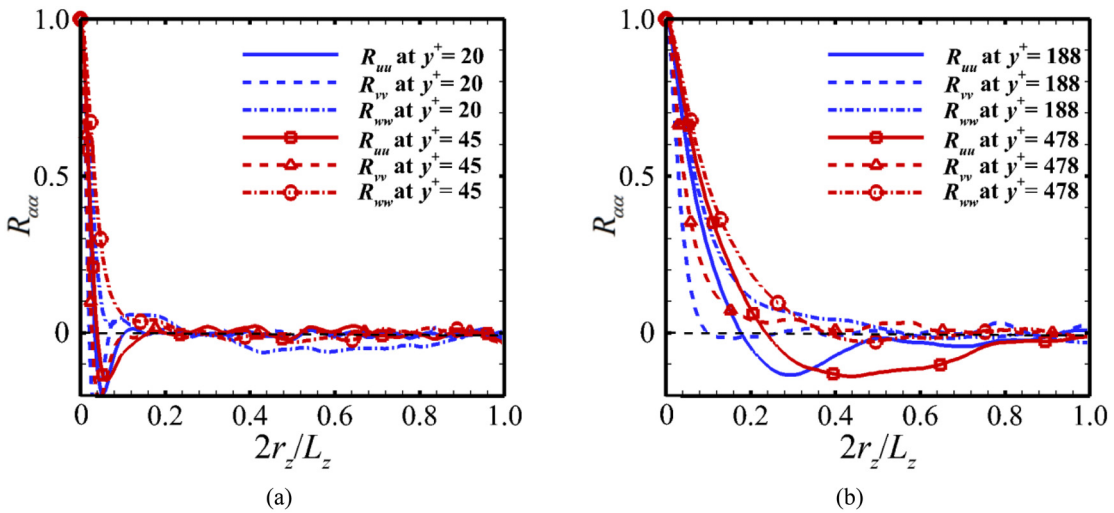

FIG. 3. Spanwise two-point correlation coefficient distributions at four wall-normal locations when $x = 0.2\delta_{in}$: (a) $y^+ = 20$ and 45; (b) $y^+ = 188$ and 478. R_{uu}: streamwise velocity; R_{vv}: wall-normal velocity; and R_{ww}: spanwise velocity.

Downloaded from http://pubs.aip.org/aip/pof/article-pdf/doi/10.1063/5.0113514/16584511/105109_1_online.pdf

Published under an exclusive license by AIP Publishing

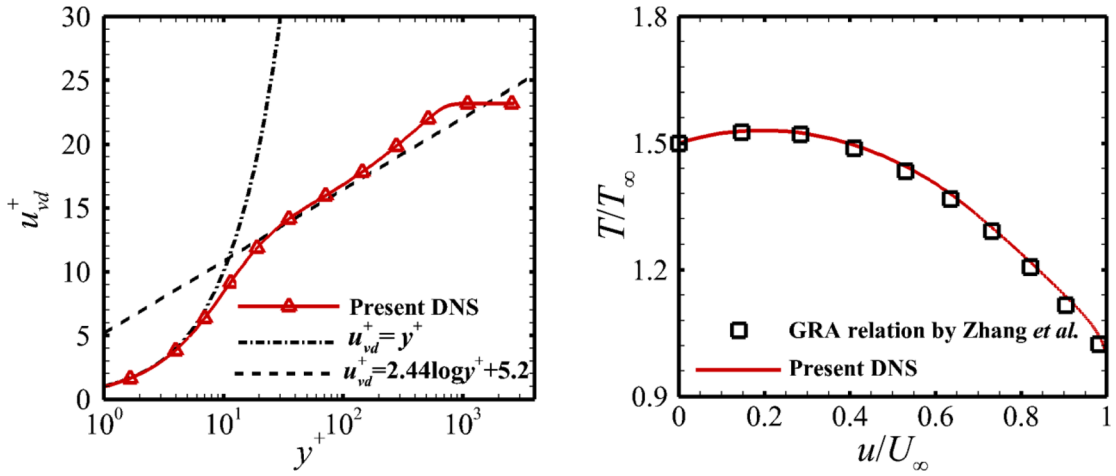

FIG. 4. Mean flow properties of the upstream turbulent boundary layer at x_{ref}: (a) profile of the van Direst transformed mean velocity u_{vd}^+ plotted against y^+ and (b) the temperature–velocity relationship.

The boundary layer thickness δ at x_{ref} is determined by the point at the 99% free-stream velocity and estimated as $\delta = 2.5\delta_{in}$. The friction Reynolds number is $Re_\tau = 769$. To validate the simulation of the upstream turbulent boundary layer, we compare the mean velocity profile and turbulence statistics to existing results and theories in Figs. 4 and 5. As shown in Fig. 4(a), the van Driest transformation is applied to the calculated mean streamwise velocity and the transformed velocity u_{vd}^+ obeys the law of the wall, with a liner scaling at $y^+ < 6$ and a logarithmic scaling at $30 < y^+ < 100$. The temperature– velocity relationship is plotted in Fig. 4(b) together with the generalized Reynolds analogy (GRA) proposed by Zhang *et al.*,[36] where satisfactory agreement is observed. In Fig. 5(a), the density-scaled root mean square (RMS) fluctuations of velocity components are plotted using outer scaling. Throughout this paper, δ denotes the boundary layer thickness taken at x_{ref}. Clearly, the computed turbulence intensities agree well with the low-speed experimental data of Erm and Joubert[37] and the DNS results of Pirozzoli *et al.*[38] The streamwise component peaks at $u_{rms}^+ \approx 2.92$ and $y^+ \approx 15$. Following Lumley,[39] the anisotropy of the Reynolds stress tensor $b_{ij} = \widetilde{u''_i u''_j}/\widetilde{u''_i u''_i} - 1/3\delta_{ij}$ is reported in Fig. 5(b) to evaluate the turbulent state. The second and third invariants of the stress anisotropy tensor, denoted as II_b and III_b in the figure, highlight a two-component turbulent state in the inner region and

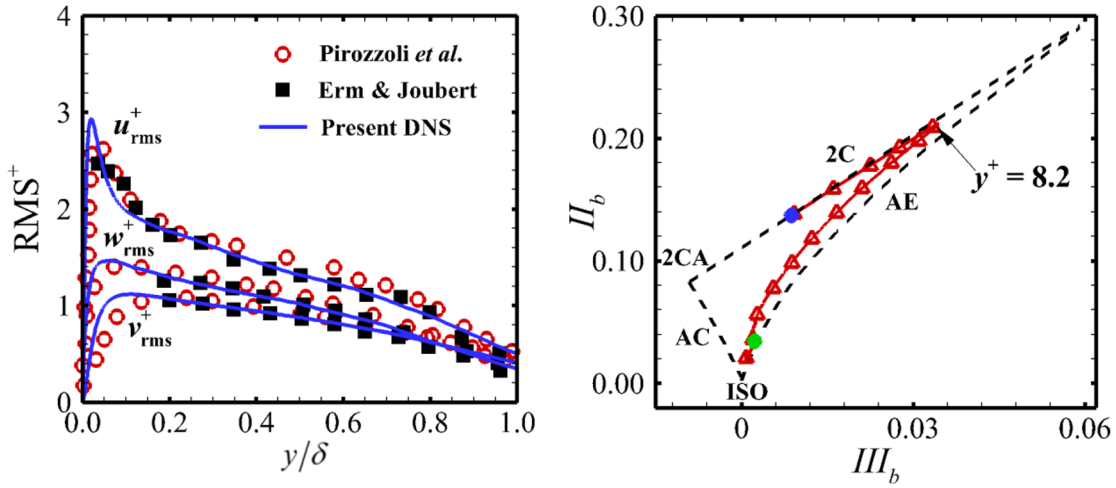

FIG. 5. Turbulence statistics of the upstream turbulent boundary layer at x_{ref}: (a) density-scaled root-mean-squared velocity fluctuations plotted against y/δ and (b) the anisotropy invariant map. The blue and green solid circles in (b) denote the first point above the wall and the point at the boundary layer edge, respectively. 2C: two-components; 2CA: two-component axisymmetric; AE: axisymmetric expansion; ISO: isotropic; and AC: axisymmetric compression.

Downloaded from http://pubs.aip.org/aip/pof/article-pdf/doi/10.1063/5.0113514/16584511/105109_1_online.pdf

Published under an exclusive license by AIP Publishing

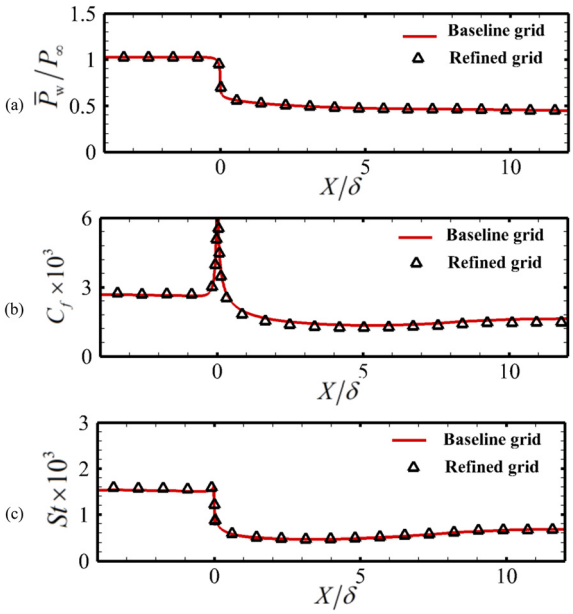

FIG. 6. Grid-sensitivity study with respect to the mean properties: (a) wall pressure $\bar{p}_w/p_\infty$; (b) skin friction coefficient $C_f = 2(\mu\partial\bar{u}/\partial y)_w/\rho_\infty u_\infty^2$; and (c) Stanton number $St = (k\partial\bar{T}/\partial y)_w/\rho_\infty U_\infty C_p(T_r - T_w)$.

an isotropic state in the outer region. In particular, the anisotropy attains its peak in the buffer layer at $y^+ = 8.2$, which is quite close to the value identified in numerical studies performed by Pasquariello *et al.*[40] and Sun *et al.*[34] for compressible turbulent boundary layers. The assessment of the statistical properties of the inflow turbulence confirms that a fully developed turbulent boundary layer is generated accurately before the expansion corner.

Finally, the sensitivity of the DNS results to the grid resolution is assessed via grid refinement. In the refined grid, the number of nodes is increased by 50% in both the x and z directions. A direct comparison to the results obtained using the refined grid is shown in Fig. 6, where the streamwise distributions of the mean wall pressure, skin friction coefficient, and Stanton number are reported. Across the expansion region, both the wall pressure and Stanton number drop sharply, whereas the skin friction coefficient exhibits a strong spike near the point of the corner due to the surface geometry change, as found previously by Fang *et al.*[13] The overall evolution in the baseline and refined grids coincides, and no significant deviations are observed upstream or downstream of the corner. This confirms that a grid convergence is obtained in the present simulation.

III. RESULTS AND DISCUSSION

A. Instantaneous and mean fields

An instantaneous flow field with density ρ/ρ_∞ in the X–Y plane at $Z = 0$, reported in Fig. 7(a), shows that the density of the incoming boundary layer decreases dramatically during the expansion process and the boundary layer becomes thicker. This is quite similar to the schlieren images of Dawson *et al.*[18] for turbulent flow over a 14° centered expansion. In Figs. 7(b)–7(d), three cross-sectional planes are shown to visualize the evolution of the instantaneous temperature field. Here, we present one plane at x_{ref}, one plane at $X = 1$ just after the expansion, and another plane at $X = 7$. As shown in Fig. 7(b), the upstream boundary layer is characterized by highly intermittent bulges in the outer layer. This is observed often in experiments and DNS

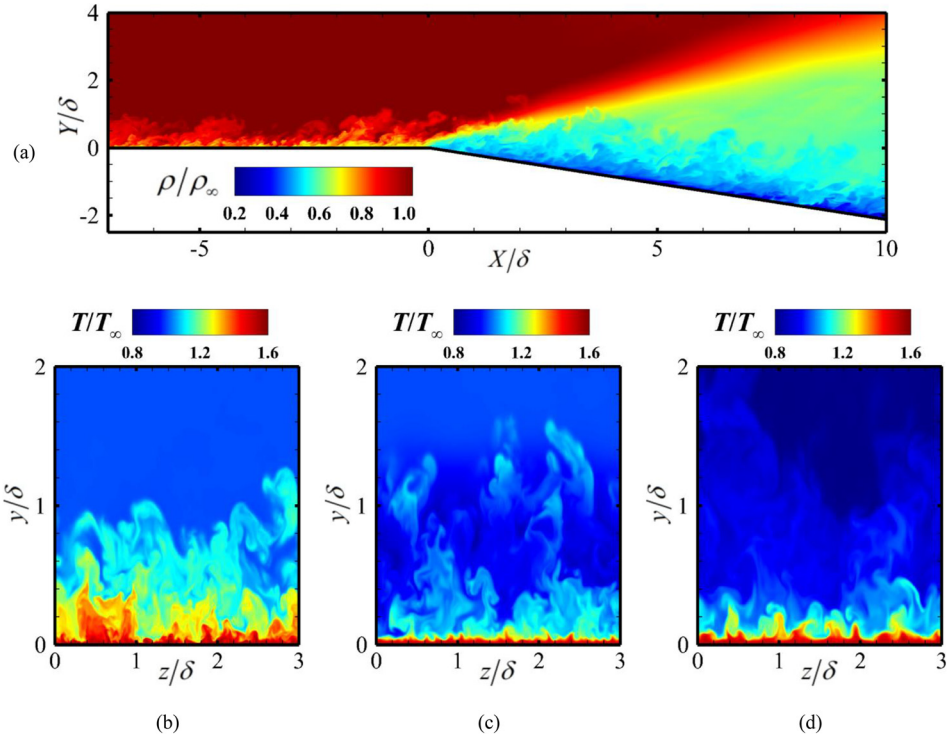

FIG. 7. (a) Contour of the instantaneous density field in the X–Y plane at $Z = 0$. (b)–(d) Contours of the instantaneous temperature fields at three cross-sectional planes: (b) x_{ref}; (c) $X = 1$; and (d) $X = 7$.

Downloaded from http://pubs.aip.org/aip/pof/article-pdf/doi/10.1063/5.0113514/16584511/105109_1_online.pdf

Published under an exclusive license by AIP Publishing

results for turbulent boundary layers.[11,12,32] In Fig. 7(c), the turbulent bulges survive at $X=1$, but quenching of the inner high-temperature small-scale structures and survival of the outer low-temperature large-scale structures are observed. This leads to the formation of a much more highly intermittent boundary layer just after the expansion. This is consistent with the visualization obtained via the filtered Rayleigh scattering technique in a Mach 3 experiment of a 14° expansion by Arnette *et al.*[11] As expected, the low-temperature, large-scale structures in the outer layer experience significant increases in scale in response to the strong density field decrease, as shown in Fig. 7(a). This phenomenon was discussed previously by Arnette *et al.*[11] In Fig. 7(d), different recovery behaviors in the inner and outer regions are seen at $X=7$. Clearly, the small-scale, high-temperature structures in the inner region recover gradually. In contrast, recovery of the large-scale, low-temperature structures in the outer region is much slower.

Figure 8 shows an instantaneous streamwise velocity field u/U_∞ in the X–Z plane at $y^+=8.2$. The velocity field at $X<0$ features a typical streaky pattern, in which alternating stripes of low- and high-speed flows are found in the spanwise direction, as a result of well-known sweep and ejection motions. The streak width, determined by the two-point fluctuating velocity correlations (not shown here), is $\Delta z^+ \approx 58$. Downstream of the expansion, it is clear that the fluctuating velocity is reduced overall and the streaky structures are essentially preserved, but the streak width increases significantly and high-speed spots inside the streaks are observed rarely at $0<X<5$. At $X=10$, the streak width is estimated to be $\Delta z^+ \approx 92$. A similar observation of an increased streak width in a DNS expansion corner was also reported by Sun *et al.*[14] at a deflection angle of 4°.

A general view of the mean flow properties throughout the expansion is presented in Fig. 9. The streamwise velocity and temperature profiles at various streamwise locations are reported as functions of the wall-normal distance y/δ. Figure 9(a) shows that the velocity profiles in the outer region become fuller than that at x_{ref} after the expansion corner and the velocity is increased over most of the boundary layer. This is an obvious consequence of acceleration during the expansion process. A considerable reduction in the inner velocity is noted at $y/\delta<0.05$, which is better seen in the figure insert. Such a velocity reduction was also observed by Sun *et al.*[14] for a supersonic flow over a 4° expansion corner. The high momentum in the free stream was inhibited from spreading into the inner layer because of turbulence decay in the outer region and the fullness level close to the wall was therefore anticipated to suffer a decrease. Different from the velocity profiles, the three downstream temperature profiles in Fig. 9(b) confirm an overall decreasing trend inside the expanded boundary layer. In the figure insert, the inner peak is sustained in the expansion region although the peak location moves slightly. The peak value and temperature gradient at the wall are both reduced. Another key observation is that the decrease in temperature at $y/\delta>0.04$ is strengthened substantially by the expansion. At $X/\delta=8$, the temperature falls from $T/T_\infty \approx 1.38$ at $y/\delta=0.04$ to $T/T_\infty \approx 1.06$ at $y/\delta=0.2$, whereas $T/T_\infty \approx 1.25$ at $y/\delta=0.2$ for the upstream flow. In addition, it is seen from Fig. 9(c) that the mean temperature profiles at $X=2$ and 8 normalized by the free-stream temperature and velocity only agree with the GRA relation[36] in the inner region, but remarkable deviations are clearly observed in the outer region. In Fig. 9(d), the profiles are re-plotted, where the temperature and velocity at the local boundary layer edge (T_e and U_e) are used for normalization. At $X=2$, the GRA in the outer layer still shows a large overshoot, however; good collapse of the mean temperature profile onto the theoretical prediction is clearly observed at $X=8$ across the boundary layer.

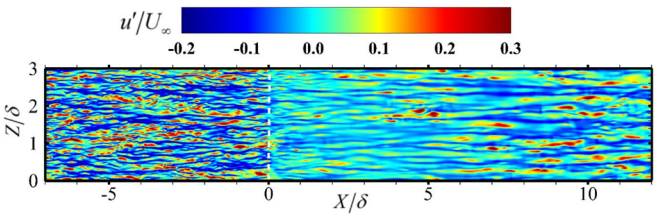

FIG. 8. Contour of the instantaneous streamwise velocity fluctuations in the X–Z plane at $y^+=8.2$. The tip of the expansion corner is denoted by the white dashed line at $X/\delta=0$.

B. Statistical properties of WHF fluctuations

We seek to provide an overview of the effect of expansion on the fluctuating WHF, a representative instantaneous field of the WHF fluctuations q', which is calculated as

$$q'(X,Z,t)=q(X,Z,t)-\overline{q(X,Z,t)}=k\left.\frac{\partial T(X,y,Z,t)}{\partial y}\right|_{\mathrm{w}}-\overline{k\left.\frac{\partial T(X,y,Z,t)}{\partial y}\right|_{\mathrm{w}}}, \quad (1)$$

is reported in Fig. 10. For a better comparison, the fluctuations are normalized using the local mean WHF $\bar{q}$. The contour of q' presents clear streaky patterns upstream and downstream of the corner. This suggests that the structural distribution of the fluctuating WHF is not changed substantially by the expansion and the streamwise coherence remains dominant. However, the main difference is seen from the characteristic length scale in the post-expansion region, which increases significantly in both the x and z directions. Correspondingly, the scales of the high-amplitude q' region become much larger. This observation will be extended and quantified in the subsequent conditional analysis. In this section, to quantify the statistical properties of the fluctuating WHF throughout the expansion, the results at four streamwise locations are studied comparatively via a detailed analysis of probability density function (PDF), pre-multiplied frequency spectrum, and space-time correlation. Here, one point is located at x_{ref} in the upstream boundary layer, and another three points are selected at $X=2$, 5, and 8 in the expanded boundary layer, denoted as S1–S3 in Fig. 10.

In Fig. 11(a), the PDFs of WHF are plotted on a logarithmic scale to emphasize the tail region. As we can see, the PDF shape is actually unchanged by the effect of expansion. All of the PDFs are positively skewed, but the negative and positive tails of the PDFs become wider at S1–S3. This suggests that extreme q events are observed more often after the expansion corner. Similar to the WHF fluctuations in a supersonic shock wave/turbulent boundary layer interaction by Tong *et al.*,[31] we observe that the PDFs of the fluctuating WHF at various streamwise locations in Fig. 11(b) exhibit good tail collapse, except for the positive tail of S1, when the local RMS value $q_{\mathrm{rms}}=\sqrt{\overline{q'(X,Z,t)^2}}$ is used for normalization. Such a behavior can be understood better from the figure insert, in which the PDFs are re-plotted on a linear scale. At S1, the PDF shape is affected heavily by the expansion,

Downloaded from http://pubs.aip.org/aip/pof/article-pdf/doi/10.1063/5.0113514/16584511/105109_1_online.pdf

Published under an exclusive license by AIP Publishing

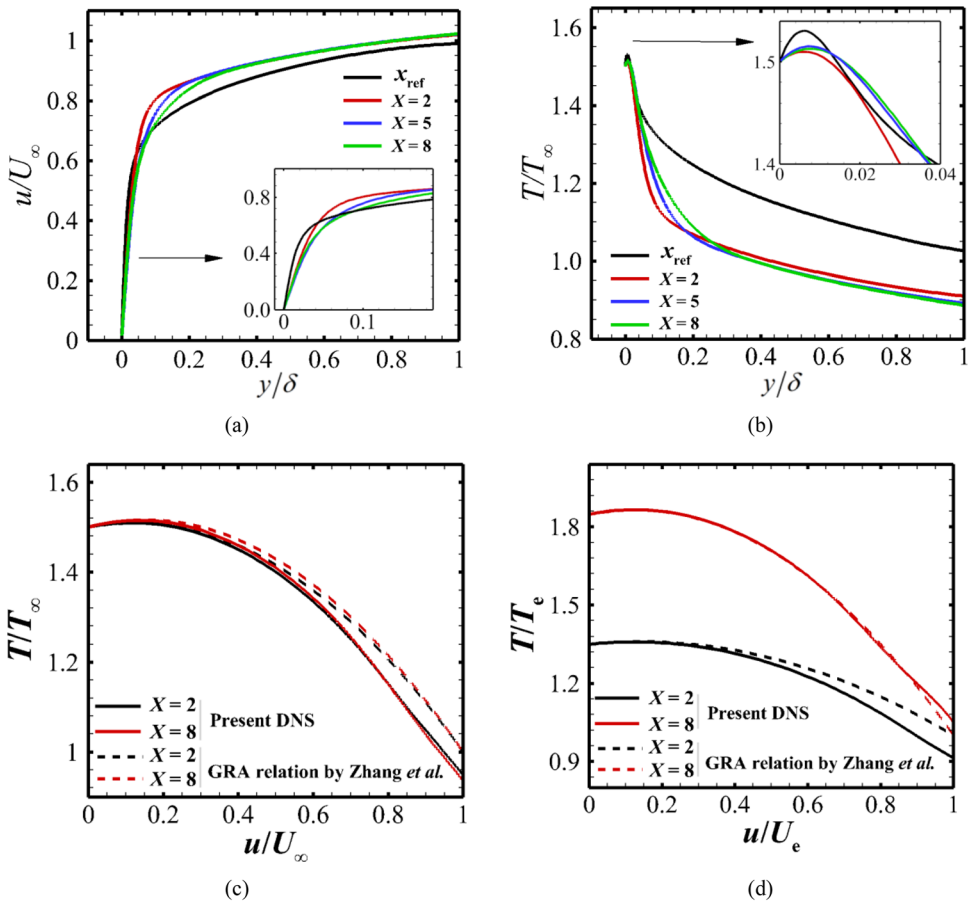

FIG. 9. Mean profiles at four streamwise locations: (a) streamwise velocity and (b) temperature. The insets in (a) and (b) present enlargements of the inner parts of the profiles. The temperature–velocity relationships at $X = 2$ and $X = 8$ are normalized by (c) the free-stream velocity and temperature (U_∞ and T_∞) and (d) the local external velocity and temperature (U_e and T_e).

where the negatively skewed distribution is greatly relieved and the peak location moves closer to zero. This results in a nearly symmetrical behavior just downstream of the expansion. The PDF at S2 exhibits relaxation toward that of x_{ref} and no obvious differences are found at S3. It is worth noting that the normalized PDFs at $-2 < q'/q_{rms} < 4$ match well with the wall shear stress fluctuations in the low-speed wall-bounded flow experiments by Nottebrock *et al.*[41] at $Re_\theta = 4420$,

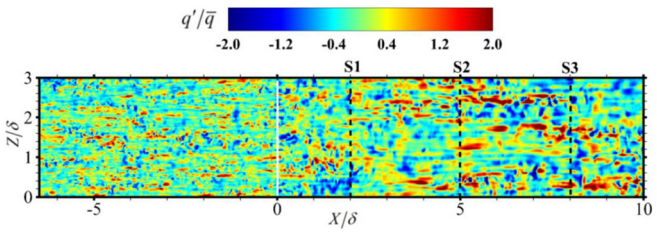

FIG. 10. Contour of the instantaneous WHF fluctuations. The white, solid line denotes the tip of the expansion corner. The three downstream streamwise locations are indicated by S1–S3.

Grosse and Schröder[42] at $Re_H = 15\,000$ (based on the duct height), and Sreenivasan and Antonia[43] at $Re_D = 6050$ (based on the channel half-height). This suggests a weak compressibility effect in the present study.

To investigate the influence of expansion on the WHF fluctuation energy distribution in frequency space, we report in Figs. 12(a) and 12(b), respectively, the pre-multiplied spectra of the wall pressure and WHF at various streamwise locations as functions of the normalized angular frequency $\omega\upsilon_w/u_\tau^2$. Welch's algorithm is used with a hamming window to estimate the power spectral density $\Psi(\omega)$, which is averaged in the z direction and scaled with respect to the square of the local RMS value (q_{rms}^2 or p_{rms}^2). The kinematic viscosity at the wall υ_w and the friction velocity u_τ are both taken at x_{ref}. In Fig. 12(a), it is seen from the wall pressure spectra at S1 that the low-frequency components of the spectrum for $\omega\upsilon_w/u_\tau^2 < 0.05$ are enhanced remarkably by the expansion, whereas the energy at the high-frequency end for $\omega\upsilon_w/u_\tau^2 > 0.2$ is relatively attenuated. As the expanded boundary layer develops downstream, there is a considerable decrease in the elevated low-frequency spectrum energy. As a result, it approaches the upstream value. The figure qualitatively supports wall pressure

Downloaded from http://pubs.aip.org/aip/pof/article-pdf/doi/10.1063/5.0113514/16584511/105109_1_online.pdf

Published under an exclusive license by AIP Publishing

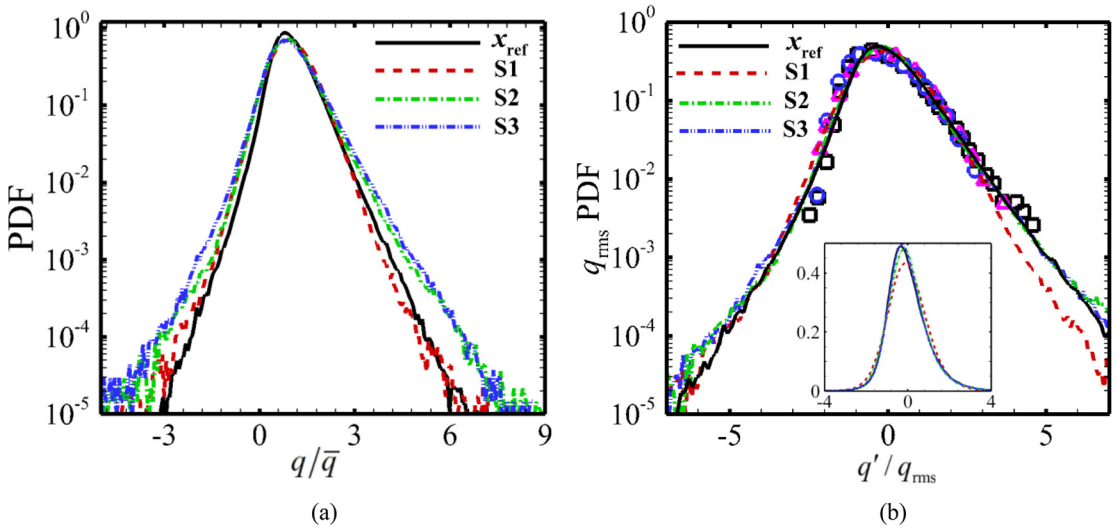

FIG. 11. (a) PDFs of WHF at various streamwise locations are made non-dimensional using the local mean value. (b) PDFs of WHF fluctuations at various streamwise locations are made non-dimensional using the local RMS value. The inset in (b) shows the PDFs re-plotted on a linear scale. Squares: Grosse and Schroder,[42] triangles: Nottebrock *et al.*,[41] circles: Sreenivasan and Antonia.[43]

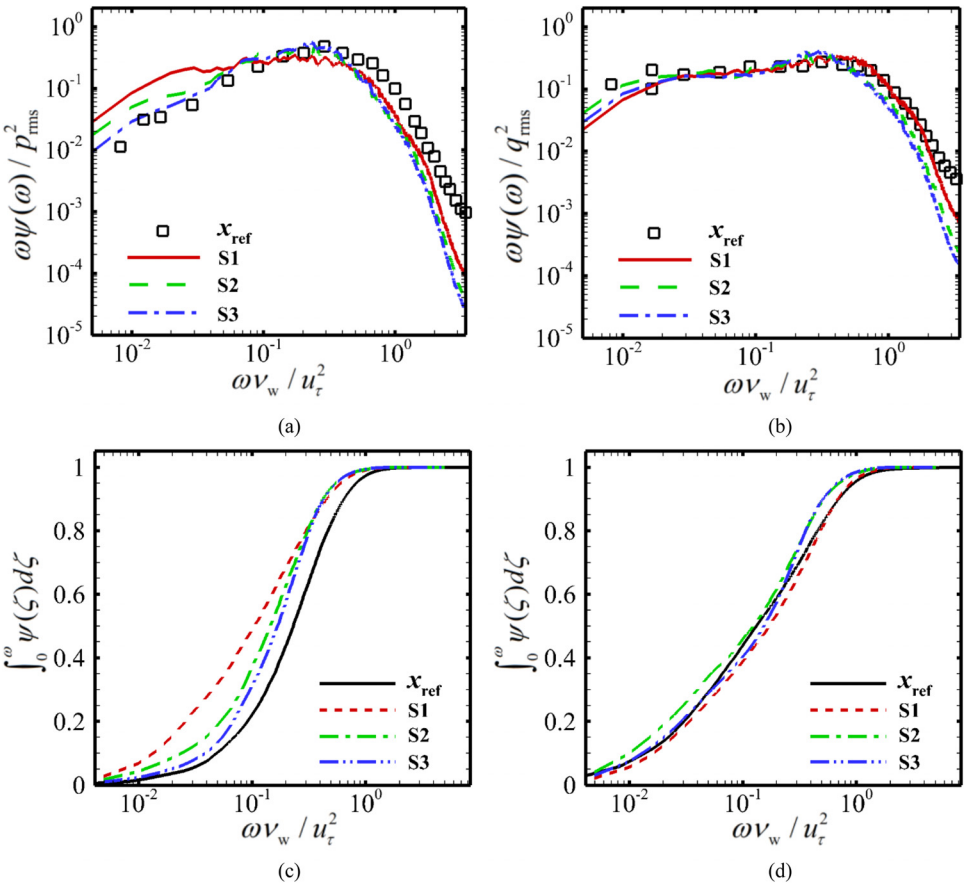

FIG. 12. (a) and (b) Pre-multiplied spectra of fluctuations at various streamwise locations and (c) and (d) integration of spectra: (a) and (c) wall pressure; (b) and (d) WHF. The spectra are scaled with respect to the square of the local RMS values and the angular frequency is in inner scale.

Downloaded from http://pubs.aip.org/aip/pof/article-pdf/doi/10.1063/5.0113514/16584511/105109_1_online.pdf

Published under an exclusive license by AIP Publishing

measurements in supersonic centered expansion corners performed by Dawson *et al.*,[18] who stated that the power spectra just downstream of the expansions shift to lower frequencies than those upstream. However, a completely different picture is presented in Fig. 12(b), where the effect of expansion exhibits little influence on the low-frequency energy in the WHF spectra and no shift to lower frequencies is observed at S1–S3. The most notable feature in the spectrum is the weak attenuation of the high-frequency components when $\omega\upsilon_w/u_\tau^2 > 0.4$. Variation in the spectral energy across the expansion is better quantified in Figs. 12(c) and 12(d) by inspecting the integrated spectra below a specific frequency ω, which is defined as $\int_0^{\omega}\psi(\zeta)d\zeta$. As shown in Fig. 12(c), the curve at S1 is shifted substantially to the left relative to x_{ref}. This is a good indicator of low-frequency energy amplification within the wall pressure spectra. In the $\omega\upsilon_w/u_\tau^2 < 0.05$ range, the portion that represents fluctuating energy is only 10% at x_{ref}, but this increases to 32% at S1 and further drops to 19% at S2 and 13% at S3. In contrast, Fig. 12(d) shows that all of the curves at the low-frequency end change slightly, with nearly 30% of the spectral energy stored in the low-frequency end ($\omega\upsilon_w/u_\tau^2 < 0.05$). Although the reason for this is not clear, this behavior might be linked to dissimilarities between the wall pressure and the WHF fluctuations. It is believed that the low-frequency components in the wall pressure spectrum are associated mainly with large-scale velocity fluctuations in the outer region, while inner small-scale velocity motions are responsible for the high-frequency end of the spectrum. Due to quenching of small-scale motions in the post-expansion region, the relative contribution from the large-scale structures increases. This explains some of the enhanced low-frequency fluctuating energy. We hypothesize that the WHF fluctuations are locally linked to the temperature fluctuations in the near-wall region, which are characterized mainly by small-scale, high-frequency dynamics. As a result, suppression of the small-scale turbulence induced by dilatation leads to energy transport at the medium- and high-frequency end ($0.1 < \omega\upsilon_w/u_\tau^2 < 4.0$).

The two-point space-time correlation coefficient R_{qq} (Δx^+, Δz^+, Δt^+) at various streamwise locations, defined as

$$R_{qq}(\Delta x^+, \Delta z^+, \Delta t^+) = \frac{\overline{q'(x_0, z, t)q'(x_0+\Delta x^+, z+\Delta z^+, t+\Delta t^+)}}{\sqrt{\overline{q'(x_0, z, t)^2}}\sqrt{\overline{q'(x_0+\Delta x^+, z+\Delta z^+, t+\Delta t^+)^2}}}, \quad (2)$$

is analyzed comparatively to explore the effect of expansion on the structural properties of the WHF field, with x_o being the reference probe and Δt^+ being the time delay. Δx^+ and Δz^+ represent the spatial separation at the wall in the x and z directions, respectively. Contours of the two-point spatial correlation coefficient R_{qq} (Δx^+, Δz^+, 0) and the longitudinal space-time correlation R_{qq} (Δx^+, 0, Δt^+) at the four selected streamwise locations are displayed in Figs. 13 and 14, respectively, where the axes in the contour maps do not use the same scales for better comparison.

Clearly, at x_{ref}, the contour map in Fig. 13(a) is compact and elongated in the streamwise direction. It shows the streaky structures upstream of the expansion seen from Fig. 10. All of the contour maps at S1–S3 exhibit an elongated streamwise distribution that demonstrates the presence of streaky structures in the post-expansion region. However, the correlations in Figs. 13(b)–13(d) are expanded, which is more pronounced in the x direction at S2 in Fig. 13(c). Taking the correlation level of 0.3 as an example, the streamwise extent is $\Delta x^+ \approx 216$ at x_{ref}. It increases persistently to $\Delta x^+ \approx 276$ at S1 and $\Delta x^+ \approx 360$ at S2, but drops to $\Delta x^+ \approx 229$ at S3, which is quite close to the upstream value. The spanwise extent increases significantly at S1, where it reaches $\Delta z^+ \approx 170$, which is approximately 2.5 times the upstream value at x_{ref}. A slow recovery is observed at S2–S3, in which the spanwise extents decrease to $\Delta z^+ \approx 148$ and 130, respectively. It is confirmed that the expansion increases the characteristic length scales in the WHF field.

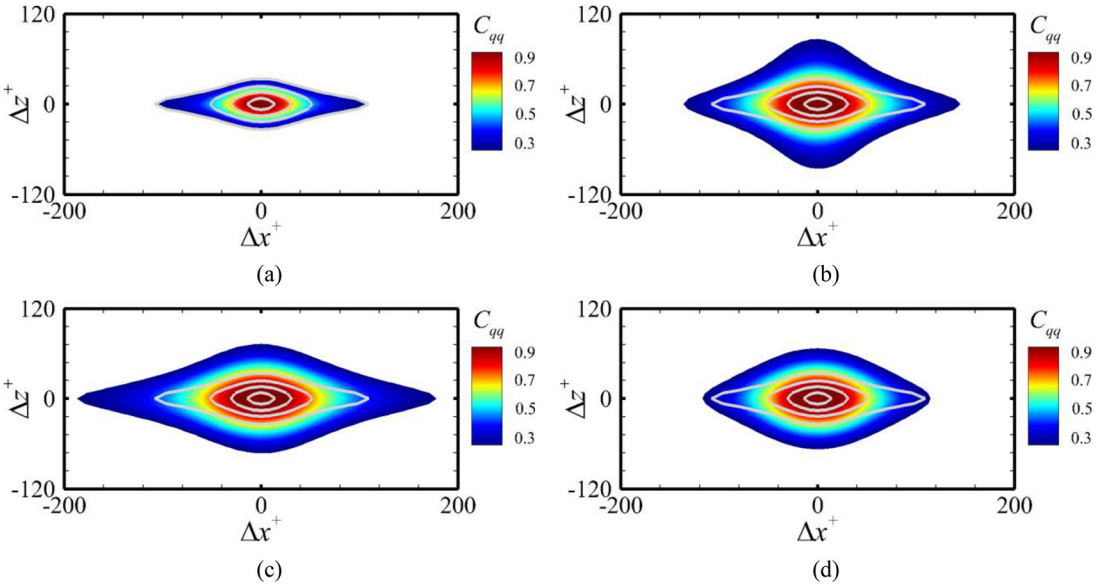

FIG. 13. Contours of the two-point spatial correlation R_{qq} (Δx^+, Δz^+, 0): (a) x_{ref}; (b) S1; (c) S2; and (d) S3. Correlation values below 0.3 are omitted. The four gray iso-lines denote the contour levels from 0.3 to 0.9 at x_{ref}, in steps of 0.2.

Downloaded from http://pubs.aip.org/aip/pof/article-pdf/doi/10.1063/5.0113514/16584511/105109_1_online.pdf

Published under an exclusive license by AIP Publishing

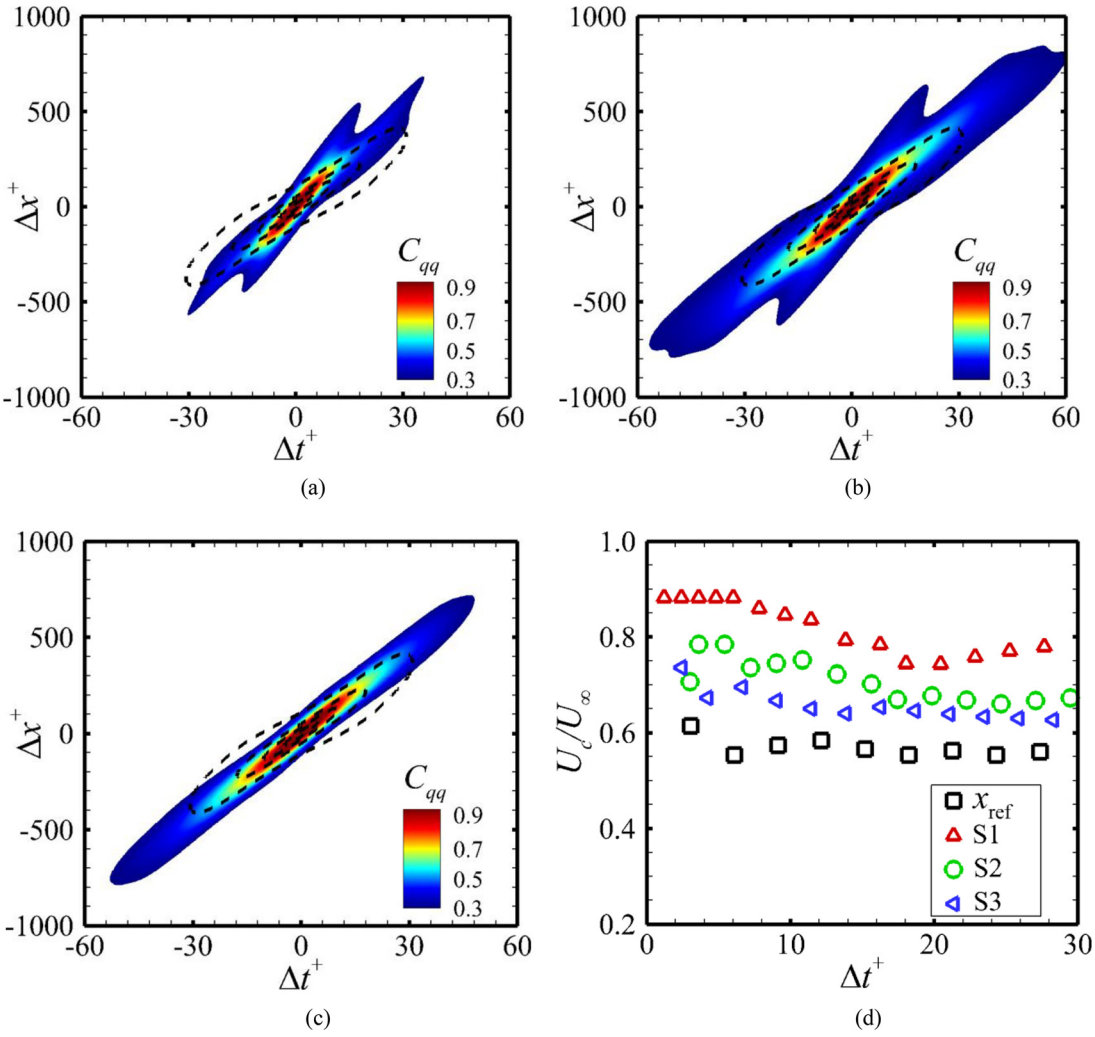

FIG. 14. (a)–(c) Contours of the space-time correlation R_{qq} (Δx^+, 0, Δt^+): (a) S1; (b) S2; and (c) S3. Correlation values below 0.3 are omitted. The four black iso-lines in (a–c) denote the contour levels from 0.3 to 0.9 at x_{ref}, in steps of 0.2. (d) Convection velocity U_c of the fluctuating WHF as a function of the time delay Δt^+.

For the upstream turbulent boundary, it is clear that the black iso-lines of R_{qq} (Δx^+, 0, Δt^+) are highly skewed. They exhibit a narrowed, forward-leaning elliptical behavior with the major axes inclined in the first and third quadrants of the $\Delta t^+ - \Delta x^+$ plane. This can be attributed to strong downstream propagation of the WHF fluctuation and is consistent with the correlation analyses of wall pressure and wall shear stress fields in compressible turbulent boundary layers.[44,45] As highlighted in Figs. 14(a)–14(c), downstream propagation of the WHF fluctuations is well preserved in the post-expansion region and a similar forward-leaning trend is observed at S1–S3. However, the effect of expansion on the space-time of the fluctuating WHF is reflected mainly in the following two respects. First, all of the correlation maps undergo systematic increases in both their spatial and temporal extents. This causes shape broadening after the expansion and indicates that the WHF fluctuation field coherence is enhanced significantly by the expansion. For example, the temporal and spatial extents for the correlation level of 0.3 at S2 in Fig. 14(b) both increase by a factor of about 2.0 with respect to the upstream values. Another important observation is the variation of the correlation map inclination. Specifically, in Fig. 14(a), the major axis at S1 rotates counterclockwise, leading to an increase in the inclination angle between the major axis and the time delay axis. At S2–S3, the inclination angle decreases consistently, whereas the major axis gradually moves close to that at x_{ref}. In Fig. 14(c), it is clear that the inclination angle at S3 remains larger than the upstream value. It is suggested that propagation of the WHF fluctuation structure generally accelerates during the expansion. This behavior can be appreciated quantitatively via inspection of the convection velocity U_c for a given time delay Δt^+. Following Duan *et al.*,[45] U_c is computed as the ratio $\Delta x^+/\Delta t^+$, with Δx^+ being the spatial separation where a local maximum of the correlation R_{qq} (Δx^+, 0, Δt^+) is obtained. Figure 14(d) shows that the WHF fluctuations at x_{ref} propagate downstream at $U_c = 0.55\,U_\infty$–$0.62U_\infty$. Obviously, the convection velocity at S1 increases significantly, reaching values in the $0.74\,U_\infty$–$0.85U_\infty$ range, and then decreases rapidly

Downloaded from http://pubs.aip.org/aip/pof/article-pdf/doi/10.1063/5.0113514/16584511/105109_1_online.pdf

Published under an exclusive license by AIP Publishing

as the probe is moved downstream, dropping to values between 0.62 U_∞ and 0.68 U_∞ at S3. As previously noted by Joen *et al.*[46] and Bernaridni and Pirozzoli,[47] large-scale fluctuations propagate faster than small-scale fluctuations. Thus, it is reasonable to conjecture that the overall higher convection velocity of the fluctuating WHF in the post-expansion region is probably linked to the significant increases in the characteristic length scales of the fluctuations, as previously discussed via the two-point spatial correlation analysis in Fig. 13.

C. Extreme WHF fluctuation events

The flow structures relevant to the extreme events of q' in the post-expansion region are investigated by analyzing the conditionally averaged fluctuation fields. Extreme events of q' in a zero-pressure-gradient supersonic turbulent boundary layer have been investigated systematically only recently and only by the present authors.[20] The present study is the first attempt to explore the effect of expansion on the flow dynamics related to extreme events of q'. Following Guerrero *et al.*,[48] extreme negative (EN) and extreme positive (EP) events of q' are defined as events where $q' < -3q_{\rm rms}$ and $q' > 3q_{\rm rms}$, respectively, with $q_{\rm rms}$ being the local RMS value of the WHF fluctuations. An instantaneous visualization of detected extreme q' events is shown in Fig. 15. Clearly, both positive and negative events are enlarged downstream of the expansion. This is qualitatively similar to the observation in Fig. 10. Since a full conditional analysis of the extreme events in the turbulent boundary layer upstream of the expansion is provided in our previous study,[20] the present work focuses on extreme events downstream of the expansion, where the conditional average is performed only in the domain $0 < X/\delta < 10$ and $0 < Z/\delta < 3$ (see Fig. 15). Specifically, an averaging box with a size ($-400 < \Delta x^+ < 400$, $0 < y^+ < 450$, $-300 < \Delta z^+ < 300$) is used to condition the flow fluctuations around an extreme event located at $\Delta x^+ = 0$, $y^+ = 0$, and $\Delta z^+ = 0$. Moreover, a domain-sensitivity study was performed by varying the domain size in the streamwise direction, but no qualitative changes are found in the conditioned fluctuation fields. This indicates that the present analysis achieves converged statistical results.

Figures 16(a) and 16(b) display the conditionally averaged q' around an EP event and an EN event, denoted as $\langle q' \rangle_{\rm EP}$ and $\langle q' \rangle_{\rm EN}$, respectively. Throughout this section, $\langle\ \rangle_{\rm EP}$ and $\langle\ \rangle_{\rm EN}$ denote the average field conditioned on an EP event and an EN event, respectively. For direct comparison, data for conditioned q' in the turbulent boundary layer upstream of the expansion reported by Tong *et al.*,[20] $\langle q' \rangle_{\rm EP} = 3q_{\rm rms}$ and $\langle q' \rangle_{\rm EN} = -3q_{\rm rms}$, are also included in the figure. In Fig. 16(a), the pattern of $\langle q' \rangle_{\rm EP}$ is unchanged by the effect of

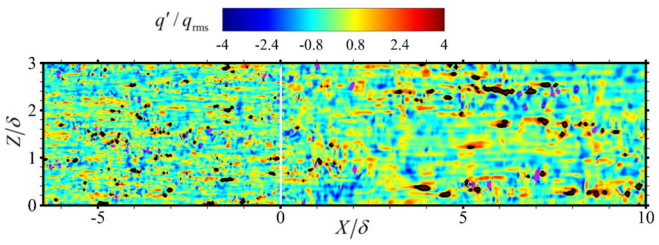

FIG. 15. Instantaneous WHF fluctuation contour normalized by the local RMS value $q_{\rm rms}$. The white, solid line denotes the tip of the expansion corner. The black and pink lines represent $3q_{\rm rms}$ and $-3q_{\rm rms}$, respectively.

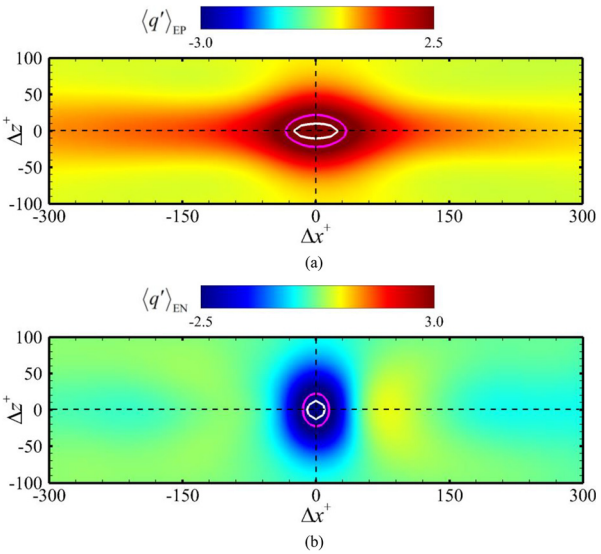

FIG. 16. Conditionally averaged q' around an extreme event at $\Delta x^+ = 0$ and $\Delta z^+ = 0$: (a) $\langle q' \rangle_{\rm EP}$; (b) $\langle q' \rangle_{\rm EN}$. Pink solid lines are the present results and white solid lines are the conditional results of Tong *et al.*[20] Solid lines in (a) and (b) denote $\langle q' \rangle_{\rm EP} = 3q_{\rm rms}$ and $\langle q' \rangle_{\rm EN} = -3q_{\rm rms}$, respectively.

expansion, and remains streamwise elongated in the expansion region, which is characterized by qualitatively similar elliptical behavior. The size of $\langle q' \rangle_{\rm EP}$ determined using $\langle q' \rangle_{\rm EP} = 3q_{\rm rms}$ is approximately 68×44 wall units in the Δx^+ and Δz^+ directions. This is much larger than the approximate size of 48×21 wall units found by Tong *et al.*[20] in the upstream turbulent boundary layer. A similar trend is observed in Fig. 16(b). $\langle q' \rangle_{\rm EN}$ exhibits a spanwise elongated elliptical distribution that resembles the upstream results of Tong *et al.*[20] quite closely, but the size of $\langle q' \rangle_{\rm EN}$ determined using $\langle q' \rangle_{\rm EN} = -3q_{\rm rms}$ is much larger in both the Δx^+ and Δz^+ directions. It is amplified by factors of approximately 1.5 and 1.9, respectively. The increased streamwise and spanwise length scales in $\langle q' \rangle_{\rm EP}$ and $\langle q' \rangle_{\rm EN}$ further support those found in the above two-point spatial correlations.

A three-dimensional view of the conditionally averaged fields is first reported in Fig. 17 to provide an overall organization of the coherent structures associated with an EP event. For better explanation, two sliced planes at $\Delta x^+ = 0$ and $\Delta z^+ = 0$ are shifted. It is interesting to note that a small region of the high-temperature flow, made visible by the red iso-surface of $\langle T^+ \rangle_{\rm EP} = 0.3$, close to the wall, emerges above the EP event, like a hot spot. This is different from the planar pattern of the high-temperature flow upstream of the expansion (see Fig. 16 in Tong *et al.*[20]). Furthermore, two interconnected tubular regions with positive temperature fluctuations, denoted by the red iso-surface of $\langle T^+ \rangle_{\rm EP} = 0.3$ in the outer region, appear on both sides above the hot spot. It is suggested that the high-temperature flow loses its coherence downstream of the expansion, which is seriously broken into the inner hot spot and the outer tubular structures. In addition, the blue iso-surface of $\langle T^+ \rangle_{\rm EP} = -1$ and the yellow iso-surface of $\langle v^+ \rangle_{\rm EP} = -0.3$ reveal that downward extrusion of the low-temperature flow is mainly responsible for the EP event generation in the expansion region, with the high-temperature flow having only a relatively passive role.

Downloaded from http://pubs.aip.org/aip/pof/article-pdf/doi/10.1063/5.0113514/16584511/105109_1_online.pdf

Published under an exclusive license by AIP Publishing

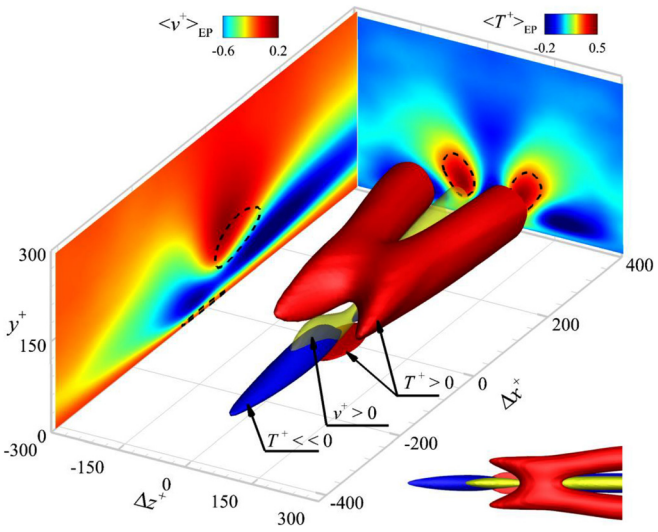

FIG. 17. Conditionally averaged three-dimensional fluctuating fields associated with an EP event at $\Delta x^+ = 0$ and $\Delta z^+ = 0$. Blue iso-surface: $\langle T^+ \rangle_{EP} = -1$; red iso-surface: $\langle T^+ \rangle_{EP} = 0.3$; yellow iso-surface: $\langle v^+ \rangle_{EP} = -0.3$; black dashed line: $\langle T^+ \rangle_{EP} = 0.3$. The insert in the lower right corner is a top view of the three-dimensional field. Conditional averages in two sliced planes at $\Delta z^+ = 0$ and $\Delta x^+ = 0$ are shifted for better visualization.

Next, we focus on the conditionally averaged fluctuations around an EP event, where Fig. 18 presents the conditionally averaged fields in the $(\Delta x^+, y^+)$ plane at $\Delta z^+ = 0$ and Fig. 19 shows the fluctuations in the $(\Delta z^+, y^+)$ plane at $\Delta x^+ = 0$. Clearly, the black streamlines in Fig. 18(a) also confirm that a strong Q4 event appears in the buffer region,

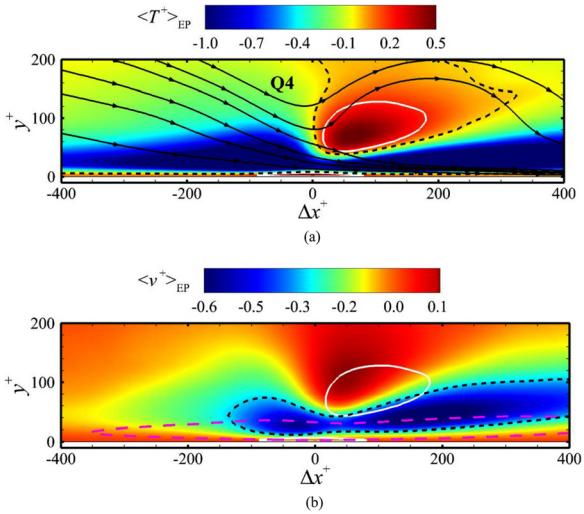

FIG. 18. Conditionally averaged fluctuations in the $(\Delta x^+, y^+)$ plane at $\Delta z^+ = 0$ associated with an EP event at $\Delta x^+ = 0$ and $\Delta z^+ = 0$: (a) temperature fluctuations with black streamlines overlapping and (b) wall-normal velocity fluctuations. The white, solid lines in (a) and (b) denote $\langle T^+ \rangle_{EP} = 0.2$. The black, dashed line in (a) denotes $\langle T^+ \rangle_{EP} = 0$. Pink and black dashed lines in (b) denote $\langle u^+ \rangle_{EP} = 2.0$ and $\langle v^+ \rangle_{EP} = -0.3$, respectively.

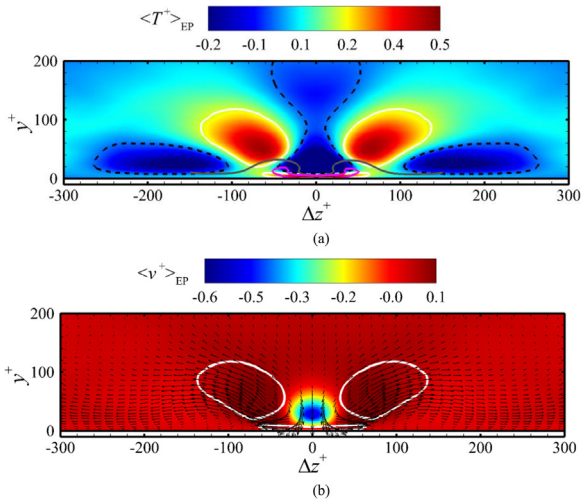

FIG. 19. Conditionally averaged fluctuations in the $(\Delta z^+, y^+)$ plane at $\Delta x^+ = 0$ associated with an EP event at $\Delta x^+ = 0$ and $\Delta z^+ = 0$: (a) temperature and (b) wall-normal velocity fluctuations. Black dashed and white solid lines denote $\langle T^+ \rangle_{EP} = 0$ and $\langle T^+ \rangle_{EP} = 0.2$, respectively. Gray and pink solid lines in (a) denote $\langle T^+ \rangle_{EP} = 0$ and $\langle T^+ \rangle_{EP} = 0.2$, from the conditional analysis of Tong *et al.*[20] Black arrows in (b) denote in-plane velocity vectors.

resulting in a region of high positive $\langle u^+ \rangle_{EP}$ [see the pink dashed line in Fig. 18(b)] and a region of high negative $\langle v^+ \rangle_{EP}$ [see the black dashed line in Fig. 18(b)] located just above the EP event at $\Delta x^+ = 0$. This finding is consistent with the conditional analysis of the EP event in the upstream turbulent boundary layer by Tong *et al.*,[20] and extremely high wall shear stress events in a turbulent pipe flow by Guerreor *et al.*[48] and in a turbulent boundary layer by Pan and Kown.[49] Figure 18(a) also reveals that the positive temperature fluctuations are concentrated mainly in the region close to the wall, while negative temperature fluctuations are observed frequently in most of the boundary layer. The result is qualitatively similar to the characteristic two-layer structure in $\langle T^+ \rangle_{EP}$ reported by Tong *et al.*[20] Such a behavior likely occurs because the overall mean temperature profile distribution is not changed essentially by the expansion [see Fig. 9(b)]. However, we remark that, even though the EP event remains surrounded by a high-temperature flow in the inner layer at $y^+ < 10$, which is in accordance with previous findings by Tong *et al.*,[20] two regions of large positive temperature fluctuations $\langle T^+ \rangle_{EP} > 0.2$ exist. One region is located just above the EP event and another is located above the region downstream of the EP event. The regions are enclosed by white solid lines in Fig. 18. Their presence suggests that flow dynamics related to the EP event are different in the post-expansion region. Importantly, the differences are highlighted in Fig. 19, where the computed $\langle T^+ \rangle_{EP}$ is compared directly to the numerical results of Tong *et al.*[20] obtained in the transverse section at $\Delta x^+ = 0$. As reported by Tong *et al.*,[20] the EP event in the upstream zero-pressure-gradient turbulent boundary layer is a product of the extrusion motion of the upper low-temperature flow, which can be interpreted vividly as a fist hitting the high-temperature flow on the wall. Furthermore, Tong *et al.*[20] suggested that even though the high-temperature flow is highly squeezed, the spanwise coherence of the high-temperature flow is destroyed only at the roll-ups of the

Downloaded from http://pubs.aip.org/aip/pof/article-pdf/doi/10.1063/5.0113514/16584511/105109_1_online.pdf

Published under an exclusive license by AIP Publishing

high-temperature flow at both the spanwise ends [see the pink solid line in Fig. 19(a)]. A careful inspection of the iso-lines of $\langle T^+\rangle_{EP}=0$ and 0.2 denoted by the white solid and black dashed lines in Fig. 19(a) and the vector plots reported in Fig. 19(b) proves that the downstream extrusion motion of the negative temperature fluctuations dominates in the post-expansion region and the low-temperature flow does not penetrate the high-temperature flow to arrive at the wall. Interestingly, there are two large regions with large magnitudes of positive $\langle T^+\rangle_{EP}$. These flank the large central region with high magnitudes of negative $\langle T^+\rangle_{EP}$. There are also two large regions with high magnitudes of negative $\langle T^+\rangle_{EP}$ distributed symmetrically in the Δz^+ direction. This scenario might be interpreted as the promotion of the extrusion motion induced by the expansion effect. Contrasting the gray solid and black dashed lines shown in Fig. 19(a), the size of the central region of negative $\langle T^+\rangle_{EP}$ becomes much larger. This can be understood intuitively as a much bigger fist hitting the high-temperature flow. As a result, the size of the highly squeezed high-temperature flow increases correspondingly. This might explain the increased $\langle q'\rangle_{EP}$ length scales observed in Fig. 16(a). On the other hand, the two large regions of positive $\langle T^+\rangle_{EP}$ at $20<y^+<120$ are extruded from the large positive temperature fluctuations above the EP event because of the promoted extrusion motion. Therefore, the occurrence of the two large regions of negative $\langle T^+\rangle_{EP}$, which are located in the $-270<\Delta z^+<-100$ and $100<\Delta z^+<270$ ranges, respectively, is a direct result of high-temperature flow ejection from the inner layer, which leads it to break through the upper low-temperature flow.

In Fig. 20, a three-dimensional view of the conditioned coherent structures associated with an EN event is displayed. A pair of counter-rotating oblique vortices is visualized using the Q criterion.[50] In the figure, we report iso-surfaces of positive and negative temperature fluctuations $\langle T^+\rangle_{EN}$ as well as the iso-surface of $Q/Q_{max}=10\%$ (Q_{max} being the global maximum value of Q), colored by the wall-normal velocity fluctuations $\langle v^+\rangle_{EN}$. Looking carefully at $\langle T^+\rangle_{EN}$, we highlight that the negative $\langle T^+\rangle_{EN}$, indicated by the blue iso-surface of $\langle T^+\rangle_{EN}=-1$, has a clear tendency to reside between the left-side clockwise and right-side counterclockwise oblique vortices, denoted as Q_L and Q_R, respectively, in the figure. In contrast, the positive $\langle T^+\rangle_{EN}$, denoted by the yellow iso-surface of $\langle T^+\rangle_{EN}=0.3$, is clustered into an elongated pipe downstream of the EN event. This flow topology can be seen in the figure insert, where the top projection in the $\Delta x^+-\Delta z^+$ plane is shown. Consistent with the EN conditional average of Tong *et al.*,[20] the distribution of $\langle v^+\rangle_{EN}$ on the iso-surface of $Q/Q_{max}=10\%$ and the rotation directions of the two oblique vortices (see the red arrows) further support that the large-scale, low-temperature structure is driven mainly by strong downwash motions between these two oblique vortices.

Likewise, the conditionally averaged fluctuation fields in the $(\Delta x^+, y^+)$ plane at $\Delta z^+=0$ around an EN event are given in Fig. 21, and the results in the $(\Delta z^+, y^+)$ plane at $\Delta x^+=0$ are reported in Fig. 22. There is an inclined large-scale structure of high negative $\langle T^+\rangle_{EN}$ marked by white solid lines in Figs. 21(a) and 22(a). This structure appears above the EN event and is accompanied by a large region of high negative $\langle v^+\rangle_{EN}$, as observed in Fig. 21(b). Unlike with the $\langle T^+\rangle_{EP}$ previously discussed in Fig. 18(a), we observe that the high-temperature structure covering the wall is seriously broken. A small region of low positive $\langle T^+\rangle_{EN}$ is present at $\Delta x^+<-80$ upstream of the EN event and a large region of high positive $\langle T^+\rangle_{EN}$ is present at $\Delta x^+>40$ downstream of the EN event. This is a manifestation of the

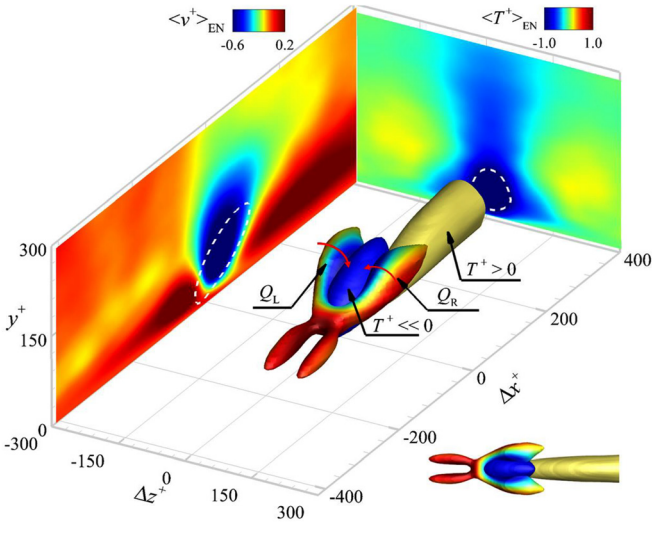

FIG. 20. Conditionally averaged three-dimensional fluctuating fields associated with an EN event at $\Delta x^+=0$ and $\Delta z^+=0$. Blue iso-surface: $\langle T^+\rangle_{EN}=-1$; yellow iso-surface: $\langle T^+\rangle_{EN}=0.3$; white dashed line: $\langle T^+\rangle_{EN}=-1$. The two oblique vortices marked as the left-side (Q_L) and right-side (Q_R) vortices are displayed according to the Q criterion ($Q/Q_{max}=10\%$) and colored by the wall-normal velocity fluctuations $\langle v^+\rangle_{EN}$. The red arrows represent the rotation direction of the oblique vortices. Two sliced planes at $\Delta z^+=0$ and $\Delta x^+=0$ are shifted.

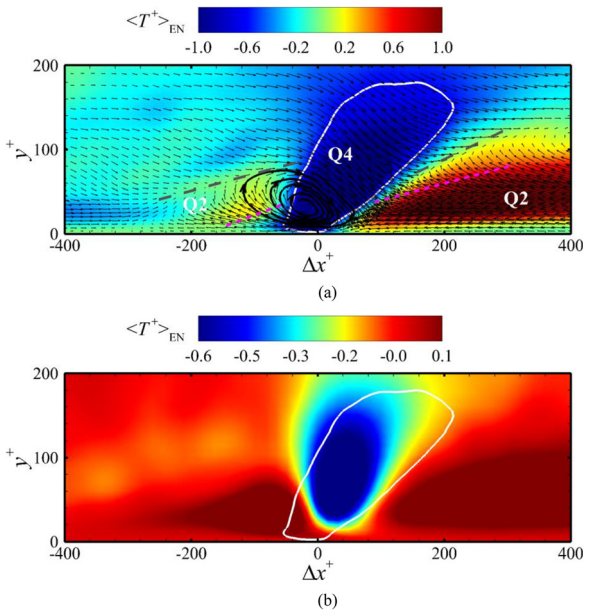

FIG. 21. Conditionally averaged fluctuations in the $(\Delta x^+, y^+)$ plane at $\Delta z^+=0$ are associated with an EN event at $\Delta x^+=0$ and $\Delta z^+=0$: (a) temperature fluctuations with overlapped vector plots and streamlines in black and (b) wall-normal velocity fluctuations. White solid lines denote $\langle T^+\rangle_{EN}=-0.6$. The Q2/Q4 interfaces are denoted by the gray and pink dashed lines. Gray: present; pink: Tong *et al.*[20]

Downloaded from http://pubs.aip.org/aip/pof/article-pdf/doi/10.1063/5.0113514/16584511/105109_1_online.pdf

Published under an exclusive license by AIP Publishing

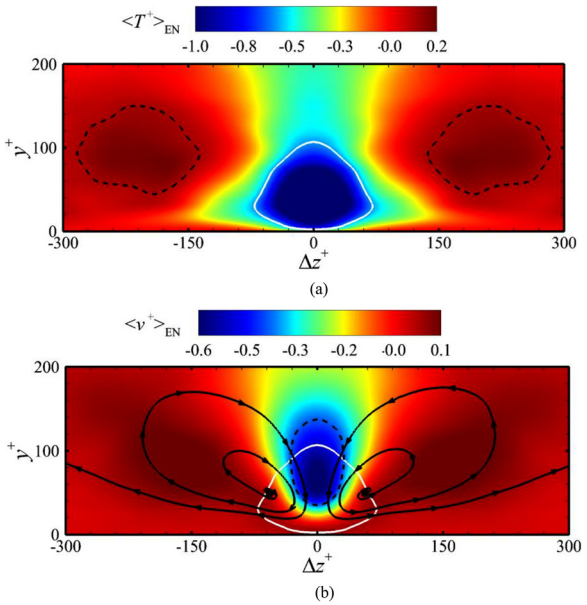

FIG. 22. Conditionally averaged fluctuations in the $(\Delta z^+, y^+)$ plane at $\Delta x^+ = 0$ associated with an EN event at $\Delta x^+ = 0$ and $\Delta z^+ = 0$: (a) temperature fluctuations and (b) wall-normal velocity fluctuations with overlapped streamlines in black. White solid lines denote $\langle T^+ \rangle_{EN} = -0.6$. Black dashed lines in (a) and (b) denote $\langle T^+ \rangle_{EN} = 0.1$ and $\langle v^+ \rangle_{EN} = -0.4$, respectively.

high-speed downward movement of the large-scale low-temperature structure, according to the converging Q4/Q2 pattern displayed by the vector plots in Fig. 21(a). As we can see, the large-scale, low-temperature structure is dominated by the sweep motion caused by the Q4 $(+u', -v')$ event, which continuously transports the outer low-temperature flow toward the wall. In contrast, the two regions of positive $\langle T^+ \rangle_{EN}$ on both sides are related to the ejection motion caused by the Q2 $(-u', +v')$ event, which in turn takes the inner high-temperature flow away from the wall. Correspondingly, there exist two inclined Q2/Q4 interfaces, which are upper front and upper rear of the EP event, denoted by the gray dashed lines in Fig. 21(a). This converging Q4/Q2 pattern has been observed previously by Lee and Sung[51] and Adrian *et al.*[52] in the streamwise/wall-normal cut through a hairpin vortex center. Moreover, comparing the interfaces to the numerical data of Tong *et al.*[20] suggests that these two interfaces are moved outward and the inclination angles are altered. Specifically, the two inclination angles in the post-expansion region are nearly 10° and 23°, respectively, compared to approximately 14° and 11° in the upstream turbulent boundary layer. Such a flow pattern can be analyzed better by examining the streamlines in Figs. 21(a) and 22(b). Clearly, a clockwise-rotating spanwise vortex is found in the $(\Delta x^+, y^+)$ plane and a pair of large-scale counter-rotating vortices is identified in the $(\Delta z^+, y^+)$ plane. These provide evidence for the existence of a pair of strong oblique vortices above the EN event. The flow structures present here are quite similar to previous findings by Cardesa *et al.*[53] in turbulent channel flow and of Bross *et al.*[54] in an adverse pressure gradient turbulent boundary layer, who found a low-momentum region and oblique vortices in the buffer region that emerges above the backflow event. Therefore, it is reasonably inferred that the EN event is a product of the high-speed impact of the large-scale, low-temperature flow on the wall, and that this impact is induced by the sweep motion between the two oblique vortices. Overall, this is consistent with the conditional analysis in Tong *et al.*[20] for the EN event in the upstream boundary layer.

D. Decomposition of the mean WHF

In previous papers by the present authors, a successful application of mean WHF decomposition was demonstrated for a zero-pressure-gradient spatially developing compressible turbulent boundary layer[20] and a reflected shock interaction.[31] The mean WHF was dominated mainly by the combined action of a particularly large positive term related to the work of the Reynolds stresses and a large negative term associated with turbulent heat transport. Using a scale-based analysis based on the BEMD method, we arrived at conclusions similar to those of the decomposition analysis of the mean WHF downstream of the interaction. The shock interaction increased the contribution of the outer large-scale structures to the mean WHF generation in the downstream region substantially.

In the present work, we perform a decomposition analysis of the mean WHF in the post-expansion region to gain useful information regarding the response of the mean WHF generation to the imposed expansion effect. Since the mean WHF decomposition in the upstream turbulent boundary layer has been analyzed in detail by Tong *et al.*,[20] the effect of expansion on the mean WHF generation is analyzed by comparing the decomposition downstream of the expansion directly to the decomposed data from Tong *et al.*[20] The decomposition formula proposed by Sun *et al.*[55] is applied in this section. This formula is derived from an integration of the compressible total energy equation under the absolute reference frame. Here, the mean WHF, calculated using the mean temperature gradient at the wall, $C_{h,\mathrm{DNS}} = k\partial\bar{T}/\partial y|_w$, is decomposed into seven terms: $C_{h,\mathrm{C}}$, $C_{h,\mathrm{TH}}$, $C_{h,\mathrm{MD}}$, $C_{h,\mathrm{TKE}}$, $C_{h,\mathrm{MS}}$, $C_{h,\mathrm{RS}}$, and $C_{h,\mathrm{G}}$, which are expressed explicitly using

$$
\begin{aligned}
C_{h,\mathrm{C}} &= \frac{1}{\rho_\infty u_\infty^4}\int_0^\infty k\frac{\partial \bar{T}}{\partial y}\frac{\partial \widetilde{u}}{\partial y}dy,\\
C_{h,TH} &= \frac{1}{\rho_\infty u_\infty^4}\int_0^\infty -c_p\bar{\rho}\widetilde{v''T''}\frac{\partial \widetilde{u}}{\partial y}dy,\\
C_{h,\mathrm{MD}} &= \frac{1}{\rho_\infty u_\infty^4}\int_0^\infty (\overline{u''\sigma_{xy}} + \overline{v''\sigma_{yy}})\frac{\partial \widetilde{u}}{\partial y}dy,\\
C_{h,\mathrm{TKE}} &= \frac{1}{\rho_\infty u_\infty^4}\int_0^\infty -\frac{1}{2}(\overline{\rho u''u''v''} + \overline{\rho v''v''v''})\frac{\partial \widetilde{u}}{\partial y}dy,\\
C_{h,\mathrm{MS}} &= \frac{1}{\rho_\infty u_\infty^4}\int_0^\infty (\widetilde{u}\bar{\sigma}_{xy} + \widetilde{v}\bar{\sigma}_{yy})\frac{\partial \widetilde{u}}{\partial y}dy,\\
C_{h,\mathrm{RS}} &= \frac{1}{\rho_\infty u_\infty^4}\int_0^\infty -\bar{\rho}(\widetilde{u}\widetilde{u''v''} + \widetilde{v}\widetilde{v''v''})\frac{\partial \widetilde{u}}{\partial y}dy,\\
C_{h,\mathrm{G}} &= \frac{1}{\rho_\infty u_\infty^4}\int_0^\infty (\widetilde{u}-u_\infty)\left[\rho\frac{D\widetilde{E}}{Dt} + \frac{\partial(\widetilde{u}\bar{p})}{\partial x} + \frac{\partial(\widetilde{v}\bar{p})}{\partial y}\right.\\
&\quad -\left(k\frac{\partial \bar{T}}{\partial x} - c_p\bar{\rho}\widetilde{u''T''} + \overline{u''\sigma_{xx}} + \overline{v''\sigma_{yx}}\right.\\
&\quad -\frac{1}{2}\overline{\rho u''u''u''} - \frac{1}{2}\overline{\rho v''v''u''} + \widetilde{u}\bar{\sigma}_{xy}\\
&\quad \left.\left.+\widetilde{v}\bar{\sigma}_{yy} - \widetilde{u}\overline{\rho u''u''} - \widetilde{v}\overline{\rho v''u''}\right)\right]dy.
\end{aligned}
\tag{3}
$$

Downloaded from http://pubs.aip.org/aip/pof/article-pdf/doi/10.1063/5.0113514/16584511/105109_1_online.pdf

Published under an exclusive license by AIP Publishing

Here, $\widetilde{E}$ is the specific total energy, σ_{xx}, σ_{xy}, and σ_{yy} denote the components of the viscous stress tensor, respectively. The terms $C_{h,C}$ and $C_{h,MD}$ represent the contributions of thermal conduction and the wall-normal component of molecular diffusion, respectively. The terms $C_{h,TH}$ and $C_{h,TKE}$ are associated with turbulent transport of heat and turbulent kinetic energy, respectively. The terms $C_{h,MS}$ and $C_{h,RS}$, respectively, denote the work of the molecular stresses and the Reynolds stresses. The term $C_{h,G}$ accounts for the variation in $\widetilde{E}$ with time, the work of pressure, and the streamwise heterogeneity.

Figures 23(a) and 23(b) report the contributions of the seven decomposed components of the mean WHF at $X=1$ and $X=8.5$, respectively. The relative errors, computed from $[C_{h,C}+C_{h,TH}+C_{h,MD}+C_{h,TKE}+C_{h,MS}+C_{h,RS}+C_{h,G}-C_{h,DNS}]/C_{h,DNS}$, are approximately 0.17% and 0.11%, respectively. This result confirms that the decomposition method in the present study is highly reliable. This behavior is different from that discussed in the previous decomposition analysis of the upstream supersonic boundary layer reported by Tong *et al.*,[20] who found that the mean WHF $C_{h,DNS}$ was dominated by the positive $C_{h,RS}$ and the negative $C_{h,TH}$, yielding up to 126.67% and −76.64% of the total WHF, respectively. As observed in Fig. 23(a), just after the expansion, the predominance of $C_{h,TH}$ and $C_{h,RS}$ is overtaken by $C_{h,C}$ and $C_{h,MS}$, respectively. Specifically, the positive $C_{h,MS}$, which is about 146.17% of $C_{h,DNS}$ mainly counteracts the negative $C_{h,C}$, which reaches approximately −95.76% of $C_{h,DNS}$. In contrast, it is seen that $C_{h,TH}$ and $C_{h,RS}$ contribute only −54.44% and 78.12% of $C_{h,DNS}$, respectively. The contributions of the other three components, $C_{h,MD}$, $C_{h,TKE}$, and $C_{h,G}$, remain negligibly small. It is highlighted that the mean WHF generation just after the expansion can be explained vividly that the excessive heat at the wall generated by the work of the molecular stress $C_{h,MS}$ is transported away from the wall by the mean heat conduction $C_{h,C}$ across the boundary layer. This phenomenon can be attributed to the relaminarization that occurs during expansion, in which the reduced turbulent fluctuations near the corner become less significant than the mean flow field, as previously discussed by Teromoto *et al.*[10] and Narasimha and Viswanath.[21] Upon recalling the expressions in Eq. (3) for $C_{h,C}$, $C_{h,TH}$, $C_{h,MS}$, and $C_{h,RS}$, the reason for the increased contributions of $C_{h,C}$ and $C_{h,MS}$, which are mainly related to the mean flow field, becomes apparent. In Fig. 23(b), this scenario is not observed at $X=8.5$, where the positive $C_{h,RS}$ and the negative $C_{h,TH}$ are the principal

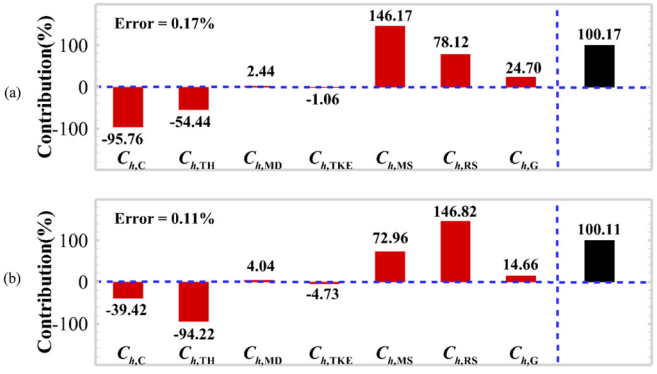

FIG. 23. Contributions of the seven decomposed components: (a) $X=1$ and (b) $X=8.5$. The black bars in (a) and (b) denote the sums of the seven decomposed components.

contributors again, contributing about 146.82% and −94.22% of $C_{h,DNS}$ respectively. This is qualitatively consistent with the observations in the previous decomposition by Tong *et al.*[20] This finding suggests that the mean WHF in the downstream region is characterized by the balance between the work of the Reynolds stresses $C_{h,RS}$ and turbulent heat transport $C_{h,TH}$. This is indicative of the great importance of the reestablishment of turbulent fluctuations inside the boundary layer.

Next, we discuss the contributions of the turbulent coherent structures to $C_{h,DNS}$ by analyzing the dominant terms $C_{h,RS}$ and $C_{h,TH}$ at $X=8.5$, since the turbulent fluctuations at $X=1$ are not the main source of the $C_{h,DNS}$ generation. According to Cheng *et al.*[56] and Tong *et al.*,[20] the velocity and temperature fluctuations in the (y^+, z) plane are both decomposed in the spanwise direction using the BEMD method. Four BEMD modes with increasing characteristic spanwise length scales, denoted by u''_i, v''_i, and T''_i, where $i=1, 2, 3, 4$ (larger subscripts indicate larger spanwise length scales), are obtained. Therefore, the wall-normal heat flux in the term $C_{h,TH}$ is rewritten as follows:

$$-\widetilde{v''T''} = -\widetilde{v''_1T''_1} - \widetilde{v''_1T''_2} - \cdots - \widetilde{v''_4T''_3} - \widetilde{v''_4T''_4}. \quad (4)$$

Substituting (4) into (3) yields

$$\begin{aligned} C_{h,TH} = &\underbrace{\frac{1}{\rho_\infty u_\infty^4}\int_0^\infty -c_p\bar{\rho}\widetilde{v''_1T''_1}\frac{\partial\widetilde{u}}{\partial y}dy}_{(1,1)} \\ &+\underbrace{\frac{1}{\rho_\infty u_\infty^4}\int_0^\infty -c_p\bar{\rho}\widetilde{v''_1T''_2}\frac{\partial\widetilde{u}}{\partial y}dy}_{(1,2)} \\ &+\cdots+\underbrace{\frac{1}{\rho_\infty u_\infty^4}\int_0^\infty -c_p\bar{\rho}\widetilde{v''_4T''_3}\frac{\partial\widetilde{u}}{\partial y}dy}_{(4,3)} \\ &+\underbrace{\frac{1}{\rho_\infty u_\infty^4}\int_0^\infty -c_p\bar{\rho}\widetilde{v''_4T''_4}\frac{\partial\widetilde{u}}{\partial y}dy}_{(4,4)}. \end{aligned} \quad (5)$$

Thus, the $C_{h,TH}$ contribution is decomposed into sixteen components, which are denoted by the mode number index (i, j). Specifically, the four diagonal components, (1, 1), (2, 2), (3, 3), and (4, 4), represent the contributions related to the first, second, third, and fourth BEMD modes of the wall-normal velocity and temperature fluctuations, respectively. It is understandable that component (1, 1) accounts for the contribution of the inner small-scale structures and component (4, 4) is related to the outer large-scale structures, while components (2, 2) and (3, 3) denote the contributions associated with intermediate-scale structures, given that the characteristic spanwise length scale grows consistently as the mode number increases. As noted by Cheng *et al.*,[56] the twelve non-diagonal components are mainly produced by interactions between structures with different spanwise length scales. Under such decomposition, the Reynolds shear stress in the term $C_{h,RS}$ is rewritten as follows:

$$-\widetilde{u''v''} = -\widetilde{u''_1v''_1} - \widetilde{u''_1v''_2} - \cdots - \widetilde{u''_4v''_3} - \widetilde{u''_4v''_4}. \quad (6)$$

Similarly, the decomposition of $C_{h,RS}$ follows:

Downloaded from http://pubs.aip.org/aip/pof/article-pdf/doi/10.1063/5.0113514/16584511/105109_1_online.pdf

Published under an exclusive license by AIP Publishing

$$C_{h,\mathrm{RS}} = \underbrace{\frac{1}{\rho_\infty u_\infty^4}\int_0^\infty -\widetilde{u}\,\overline{\rho}\,\widetilde{u''_1 v''_1}\,\frac{\partial \widetilde{u}}{\partial y}\,dy}_{(1,1)} + \underbrace{\frac{1}{\rho_\infty u_\infty^4}\int_0^\infty -\widetilde{u}\,\overline{\rho}\,\widetilde{u''_1 v''_2}\,\frac{\partial \widetilde{u}}{\partial y}\,dy}_{(1,2)} + \cdots + \underbrace{\frac{1}{\rho_\infty u_\infty^4}\int_0^\infty -\widetilde{u}\,\overline{\rho}\,\widetilde{u''_4 v''_3}\,\frac{\partial \widetilde{u}}{\partial y}\,dy}_{(4,3)} + \underbrace{\frac{1}{\rho_\infty u_\infty^4}\int_0^\infty -\widetilde{u}\,\overline{\rho}\,\widetilde{u''_4 v''_4}\,\frac{\partial \widetilde{u}}{\partial y}\,dy}_{(4,4)}. \quad (7)$$

Note that the contribution generated by the other component is less than 5% of $C_{h,\mathrm{RS}}$ and thus it is neglected in the above decomposition.

The pre-multiplied spanwise spectra of u'', v'', and T'' contained in the first two and last two modes are shown in Figs. 24 and 25, respectively. The full spectra obtained from the raw DNS data are added for comparison. Compared to those values obtained from the upstream turbulent boundary layer by Tong *et al.*,[20] the full spectra of u'', v'', and T'' peak at higher wall-normal locations and larger spanwise length scales, ($y^+ = 28$, $\lambda_z{}^+ = 218$), ($y^+ = 79$, $\lambda_z{}^+ = 182$), and ($y^+ = 44$, $\lambda_z{}^+ = 227$). This is symptomatic of the significant increases in the sizes of flow structures in the post-expansion region, as previously visualized by Humble *et al.*[12] using condensate Rayleigh scattering. The overall trends of the full spectra are captured accurately by the four BEMD modes. This suggests that the fluctuating velocity and temperature are synthesized by four groups of structures with increasing characteristic spanwise wavelengths at different wall-normal locations. In Fig. 24, the spectra of the first two modes are confined in the small (y^+, $\lambda_z{}^+$) domain, close to the inner peak in the full spectra and covering two narrow ranges of spanwise scales $\lambda_z{}^+ \approx 108$–$132$ and 218–236. In contrast, the spectra of the last two modes in Fig. 25 are concentrated in the upper right parts of the full spectra and represent outer large-scale velocity and temperature fluctuations characterized by $\lambda_z{}^+ \approx 403$–$1202$ or $\lambda_z \approx 0.53\delta$–$1.6\delta$. It is worth noting that the spectra of u'' in Figs. 25(a) and 25(d) and the spectra of T'' in Fig. 25(f) are observed to impose a footprint on the near-wall region. This reveals the wall-attached character of the outer large-scale u'' and T'' in the post-expansion region. Similar decomposed results have been found by Tong *et al.*[20] in the upstream turbulent boundary layer. The authors argued that the velocity and temperature fluctuations in the first two modes are characterized by near-wall streaks and quasi-streamwise vortices, while the last two modes reflect large-scale motion of superstructures located in the logarithmic and outer regions. However, we highlight that the characteristic spanwise scales in the spectra of the present BEMD modes are much larger than those of Tong *et al.*,[20] which is interpreted as the remnants of the increased length scales discussed in the full spectra.

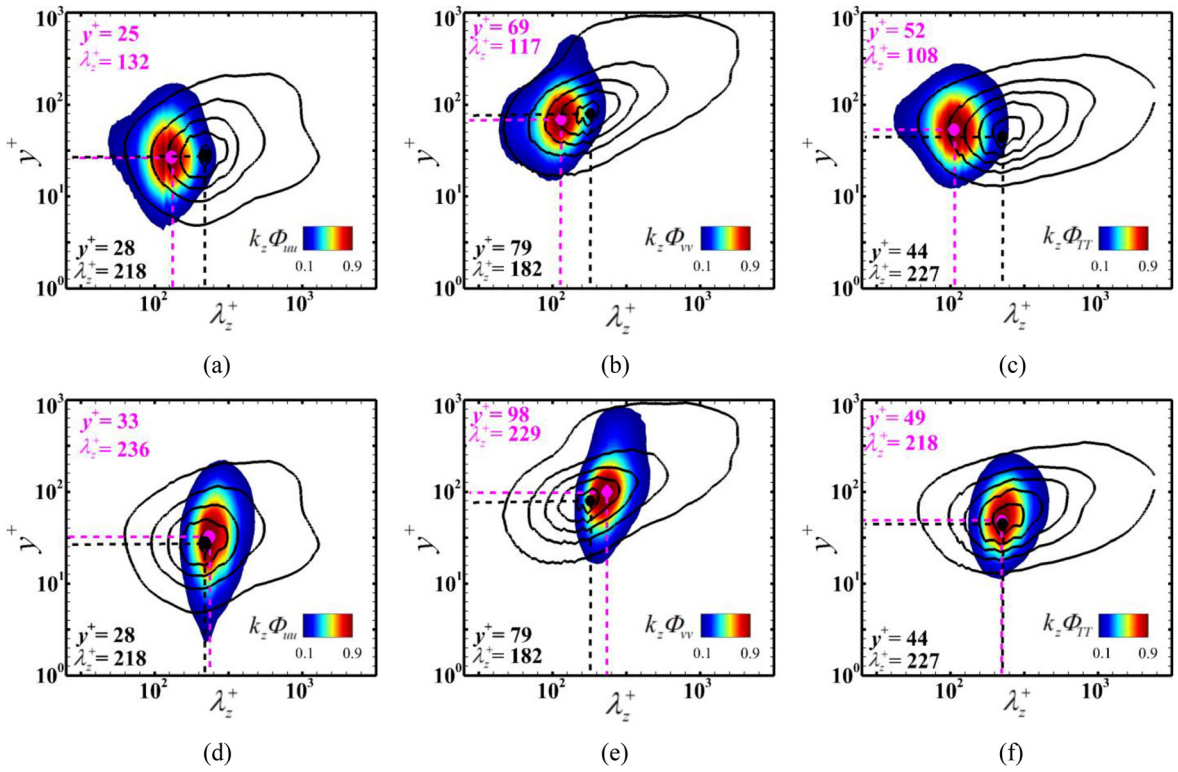

FIG. 24. Pre-multiplied spanwise spectra of the decomposed fluctuations by mode, together with the full spectra (black lines) calculated from the raw DNS data: (a)–(c) mode 1 and (d)–(f) mode 2. (a) and (c) Spectra of u''; (b) and (e) spectra of v''; and (c) and (f) spectra of T''. The spectra are normalized by their maximum values. Black lines mark five iso-lines from outward to inward at levels 0.1, 0.3, 0.5, 0.7, and 0.9. Black and pink filled circles denote the peak locations in the full spectra and each mode, respectively.

Downloaded from http://pubs.aip.org/aip/pof/article-pdf/doi/10.1063/5.0113514/16584511/105109_1_online.pdf

Published under an exclusive license by AIP Publishing

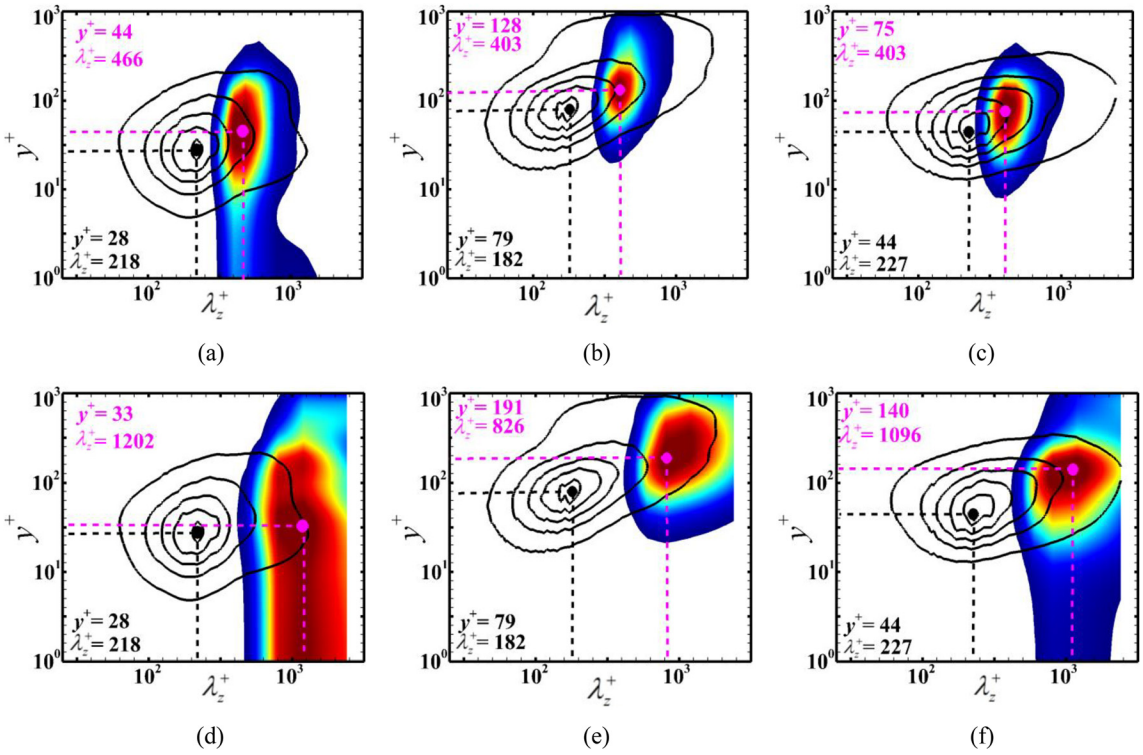

FIG. 25. Pre-multiplied spanwise spectra of the decomposed fluctuations by mode, together with the full spectra (black lines) calculated from the raw DNS data: (a)–(c) mode 3 and (d)–(f) mode 4. (a) and (c) Spectra of u''; (b) and (e) spectra of v''; and (c) and (f) spectra of T''. The spectra are normalized by their maximum values. Black lines mark five iso-lines from outward to inward at levels 0.1, 0.3, 0.5, 0.7, and 0.9. Black and pink filled circles denote the peak locations in the full spectra and each mode, respectively. For contour levels, see Fig. 24.

To provide a clear understanding of the contribution of the fluctuating velocity to the Reynolds shear stress, profiles of the sixteen decomposed components are displayed in Fig. 26 as functions of y^+. The comparison of the sum of the sixteen terms with the full profile calculated using the raw DNS data shows an excellent collapse. This confirms that the present BEMD method is highly reliable. Clearly, most of the Reynolds shear stress comes from the four diagonal components in Fig. 26(a), especially (1, 1) and (2, 2), whereas the contributions of the other twelve non-diagonal terms in Fig. 26(b) are relatively small. The dominance of the two diagonal components (1, 1) and (2, 2), peaking at approximately $y^+ \approx 37$ and 59, respectively, indicates the important role played by the inner small-scale u'' and v'' structures in the generation of the Reynolds shear stress. Similar distributions of the decomposed components and the dominance of the first two diagonal components have been reported by Tong *et al.*[20] for the decomposition of the Reynolds shear stress in the upstream turbulent boundary layer. For the wall-normal heat flux, a similar behavior is observed in Fig. 27. Among the sixteen decomposed components, (1, 1) and (2, 2) plotted in Fig. 27(a) are the two dominant contributions. This further supports the prominent role of the inner small-scale v'' and T'' structures in the wall-normal heat flux generation. The present finding is inconsistent with the decomposition of the wall-normal heat flux by Tong *et al.*,[20] who reported that the outer large-scale structures dominate the inner small-scale structures. This difference might be explained as follows. The recovery of the distorted boundary layer at $X = 8$ is incomplete. The Mach 3 experiments performed by Arnette *et al.*[7] and Dawson *et al.*[18] using 7° and 14° expansion corners found that the boundary layer was still not fully recovered after a length of 19.3δ downstream of the expansion. On the other hand, even though the large-scale structures survive the expansion process, the recovery of the dramatically weakened large-scale structures is much slower than that of the regenerated inner small-scale structures, as suggested by Sun *et al.*[14]

In Fig. 28(a), the decomposition of $C_{h,\mathrm{RS}}$ is given by the integration of the sixteen components of the Reynolds shear stress according to (7). The $C_{h,\mathrm{RS}}$ generation is dominated by the four diagonal terms, which contribute about 66.57% of $C_{h,\mathrm{RS}}$. The contributions of the first two components, (1, 1) and (2, 2), provide up to 28.22% and 25.26%, respectively. This demonstrates quantitatively the leading role of the small-scale u'' and v'' structures in the work of the Reynolds stresses. In the same way, the decomposition of $C_{h,\mathrm{TH}}$ reported in Fig. 28(b) quantifies the prominence of the four diagonal terms, which account for approximately 63.56% of turbulent heat transport. The two components (1, 1) and (2, 2) contribute approximately 20.01% and 24.76% of $C_{h,\mathrm{TH}}$, respectively. This can be compared to the 15.86% and 14.78%, respectively, reported by Tong *et al.*[20] The contribution of the component (4, 4), which is mainly linked to the outer large-scale energy-containing structures, is only 12.10%, which is much smaller than the 24.97% observed by Tong *et al.*[20] This confirms that the outer large-scale v'' and T'' structures are not the sole determinant of the

Downloaded from http://pubs.aip.org/aip/pof/article-pdf/doi/10.1063/5.0113514/16584511/105109_1_online.pdf

Published under an exclusive license by AIP Publishing

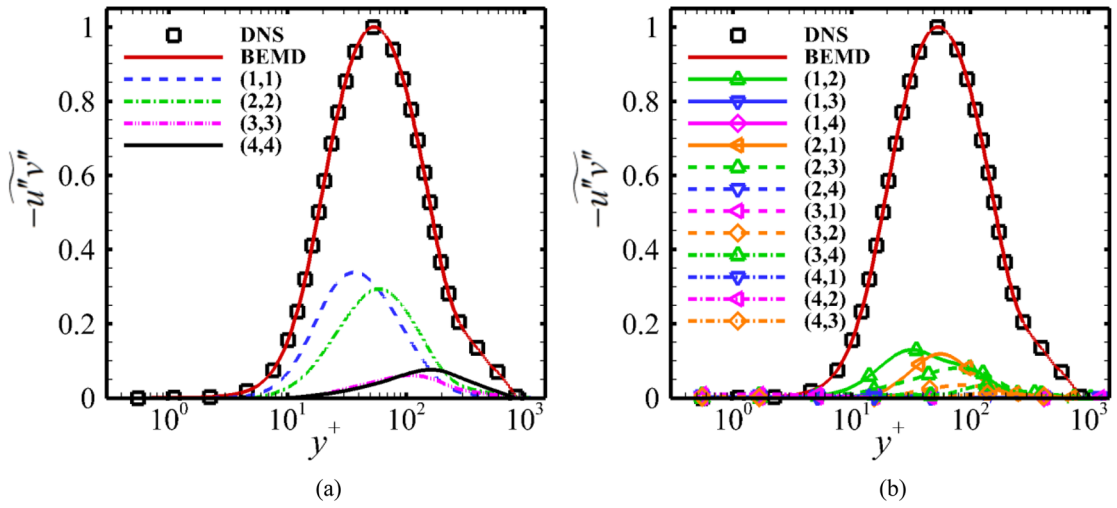

FIG. 26. Decomposed Reynolds shear stress profiles: (a) four diagonal components and (b) twelve non-diagonal components. The profiles are normalized by the maximum value of the full profile, as calculated using the raw DNS data. Squares and the red solid line denote the full profile and the sum of the sixteen decomposed components, respectively.

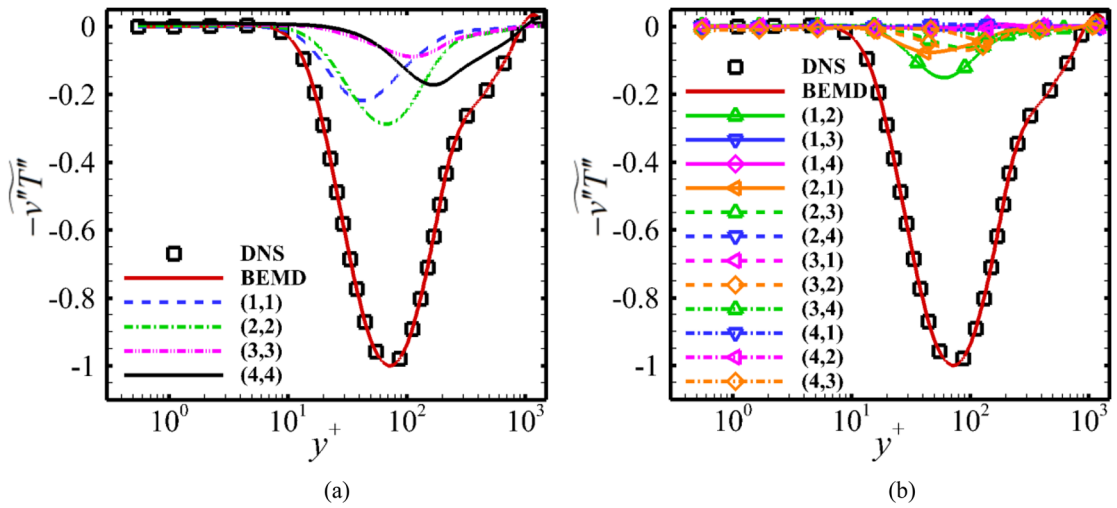

FIG. 27. Decomposed wall-normal heat flux profiles: (a) four diagonal components and (b) 12 non-diagonal components. The profiles are normalized by the maximum value of the full profile, as calculated the using raw DNS data. Squares and the red solid line denote the full profile and the sum of the sixteen decomposed components, respectively.

local contribution to the $C_{h,\mathrm{TH}}$ generation downstream of the expansion. Since $C_{h,\mathrm{RS}}$ and $C_{h,\mathrm{TH}}$ provide the dominant contributions to $C_{h,\mathrm{DNS}}$ it is important to note that a different generation mechanism of mean WHF is presented in the downstream region, where both the production and transport of heat inside the boundary layer are mostly dominated by small-scale structures with $\lambda_z^+ \approx 108$–236 in the inner region.

IV. CONCLUSIONS

The effect of expansion on wall heat flux characteristics was investigated numerically by exploiting a database provided via direct numerical simulation of a supersonic turbulent boundary layer at $M_\infty = 2.25$ and $Re_\tau = 769$ that was subjected to a 12° centered expansion corner. Expansion has significant influence on the statistical and structural properties of the fluctuating WHF. The probability density function analysis of the WHF fluctuation normalized by the local root mean square value produces good collapse of the PDF curves. In contrast to experimental observations of the wall pressure frequency spectra reported by Dawson *et al.*,[18] the pre-multiplied spectra of the fluctuating WHF do not show any evidence of low-frequency component enhancement, and the space-time WHF correlations in the post-expansion region reveal that the effect of expansion results in a significant increase in the spatial extent and the fluctuating WHF propagates downstream at $0.62\,U_\infty$–$0.85\,U_\infty$, which is much larger than the upstream convection velocity.

Downloaded from http://pubs.aip.org/aip/pof/article-pdf/doi/10.1063/5.0113514/16584511/105109_1_online.pdf

Published under an exclusive license by AIP Publishing

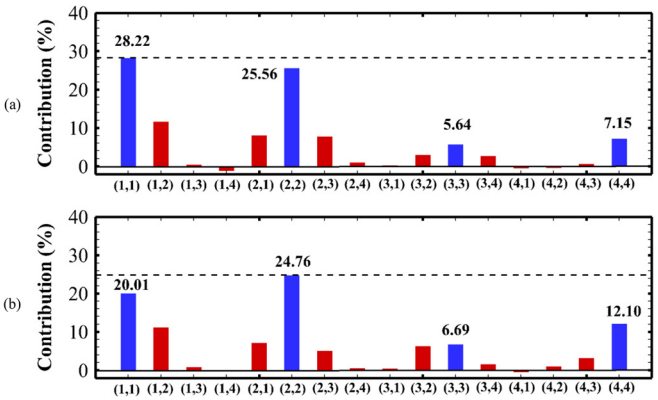

FIG. 28. Decomposition of (a) $C_{h,\mathrm{RS}}$ and (b) $C_{h,\mathrm{TH}}$. Blue bars: diagonal components; red bars: non-diagonal components.

Expansion has a clear impact on extreme WHF events. The extreme event shapes are insensitive to the expansion, but their sizes are increased considerably. Conditional analysis suggests that the EP event that emerges below a strong Q4 event is generated by the downward extrusion of low-temperature flow with the high-temperature flow above the wall having a relatively passive role. This downward movement is promoted greatly by the expansion, which destroys the integrity of the high-temperature flow dramatically. A small hot spot is located above the event, unlike with the planar pattern proposed by Tong *et al.*[20] for the generation of EP event in the upstream turbulent boundary layer. Regarding the EN event in the post-expansion region, the conditionally averaged flow fields evidence the generation mechanism previously found by Tong *et al.*[20] for the upstream turbulent boundary layer. This is interpreted as a product of the high-speed impact of large-scale, low-temperature flow on the wall, which is associated with the sweep motion between a pair of oblique vortices.

The mean WHF in the post-expansion region has been decomposed using the identity proposed by Sun *et al.*[55] The decomposed results show that the large positive $C_{h,\mathrm{MS}}$ contribution, related to the work of the molecular stresses, and the large negative $C_{h,\mathrm{C}}$ contribution, responsible for the mean heat conduction, dominate the WHF generation just after the expansion, due to the significant reduction in turbulence intensity. Downstream of the expansion, the balance between the work of the Reynolds stresses $C_{h,\mathrm{RS}}$ and the turbulent transport of heat $C_{h,\mathrm{TH}}$ dominates the generation. The BEMD method allows us to demonstrate quantitatively that the effect of expansion decreases the contribution of the outer large-scale structures to $C_{h,\mathrm{TH}}$, whereas the near-wall small-scale structures, contributing about 53.78% of $C_{h,\mathrm{RS}}$ and 44.77% of $C_{h,\mathrm{TH}}$, play a leading role in heat production and transport, respectively.

ACKNOWLEDGMENTS

This study was supported by the National Natural Science Foundation of China (Grant Nos. 11972356 and 12072306).

AUTHOR DECLARATIONS

Conflict of Interest

The authors have no conflicts to disclose.

Author Contributions

Fulin Tong: Conceptualization (equal); Writing – original draft (equal). **Siwei Dong:** Data curation (equal); Methodology (equal). **Junyi Duan:** Writing – review & editing (equal). **Xianxu Yuan:** Conceptualization (equal); Writing – review & editing (equal). **Xinliang Li:** Methodology (equal); Software (equal).

DATA AVAILABILITY

The data that support the findings of this study are available from the corresponding author upon reasonable request.

REFERENCES

[1]P. Bradshaw, "The effect of mean compression or dilatation on the turbulence structure of supersonic boundary layers," J. Fluid Mech. **63**, 449–464 (1974).
[2]K. Sreenivasan, "Laminarescent, relarminarizing and retransitional flows," Acta Mech. **44**(3–4), 1–48 (1982).
[3]C. Bourassa and F. Thomas, "An experimental investigation of a highly accelerated turbulent boundary layer," J. Fluid Mech. **634**, 359–404 (2009).
[4]E. F. Spina, "The physics of supersonic turbulent boundary layers," Annu. Rev. Fluid Mech. **26**, 287–319 (1994).
[5]J. Dussauge and J. Gaviglio, "The rapid expansion of a supersonic turbulent flow: Role of bulk dilatation," J. Fluid Mech. **174**, 81–112 (1987).
[6]D. Smith and A. Smits, "The rapid expansion of a turbulent boundary layer in a supersonic flow," Theor. Comput. Fluid Dyn. **2**, 319–328 (1991).
[7]S. Arnette, M. Samimy, and G. Elliott, "The effects of expansion on the turbulent structure of a compressible boundary layer," J. Fluid Mech. **367**, 67–105 (1998).
[8]T. T. Q. Nguyen, M. Behr, and B. U. Reinartz, "Numerical investigation of compressible turbulent boundary layer over expansion corner," AIAA Paper No. 2009-7371, 2009.
[9]M. Konopka, M. Meinke, and W. Schröder, "Large-eddy simulation of relaminarization in supersonic flow," AIAA Paper No. 2012-2978, 2012.
[10]S. Teramoto, H. Sanada, and K. Okamoto, "Dilatation effect in relaminarization of an accelerating supersonic turbulent boundary layer," AIAA J. **55**(4), 1469–1474 (2017).
[11]S. Arnette, M. Samimy, and G. Elliott, "Structure of supersonic turbulent boundary layer after expansion regions," AIAA J. **33**(3), 430–437 (1995).
[12]R. A. Humble, S. J. Peltier, and R. D. W. Bowersox, "Visualization of the structural response of a hypersonic turbulent boundary layer to convex curvature," Phys. Fluids **24**, 106103 (2012).
[13]J. Fang, Y. F. Yao, A. A. Zheltovodov, Z. R. Li, and L. P. Lu, "Direct numerical simulation of supersonic turbulent flows around a tandem expansion-compression corner," Phys. Fluids **27**, 125104 (2015).
[14]M. B. Sun, Z. W. Hu, and N. D. Sandham, "Recovery of s supersonic turbulent boundary layer after an expansion corner," Phys. Fluids **29**, 076103 (2017).
[15]F. K. Lu and K. M. Chung, "Downstream influence scaling of turbulent flow past expansion corners," AIAA J. **30**(12), 2976–2977 (1992).
[16]K. M. Chung, "Interaction region of turbulent expansion-corner flow," AIAA J. **36**(6), 1115–1116 (1998).
[17]K. M. Chung and F. K. Lu, "Damping of surface pressure fluctuations in hypersonic turbulent flow past expansion corners," AIAA J. **31**(7), 1229–1234 (1993).
[18]J. A. Dawson, M. Samimy, and S. A. Arnette, "Effects of expansions on a supersonic boundary layer: Surface pressure measurements," AIAA J. **32**(11), 2169–2177 (1994).
[19]A. W. Bloy, "The expansion of a hypersonic turbulent boundary layer at a sharp corner," J. Fluid Mech. **67**, 647–655 (1975).
[20]F. L. Tong, S. W. Dong, J. Lai, X. X. Yuan, and X. L. Li, "Wall shear stress and wall heat flux in a supersonic turbulent boundary layer," Phys. Fluids **34**, 015127 (2022).
[21]R. Narasimha and P. R. Viswanath, "Reverse transition at an expansion corner in supersonic flow," AIAA J. **13**(5), 693–695 (1975).
[22]M. D. Koll, J. V. Favale, B. M. Kirchner, G. S. Elliott, and J. C. Dutton, "Flow structure identification in the near wake of an axisymmetric supersonic base flow using MEEMD," AIAA Paper No. 2017-3972, 2017.

Downloaded from http://pubs.aip.org/aip/pof/article-pdf/doi/10.1063/5.0113514/16584511/105109_1_online.pdf

Published under an exclusive license by AIP Publishing

[23]X. L. Li, D. X. Fu, and Y. W. Ma, "Direct numerical simulation of hypersonic boundary layer transition over a blunt cone with a small angle of attack," Phys. Fluids **22**, 025105 (2010).
[24]F. L. Tong, D. Sun, and X. L. Li, "Direct numerical simulation of impinging shock wave and turbulent boundary layer interaction over a wavy-wall," Chin. J. Aeronaut. **34**(5), 350–363 (2021).
[25]F. L. Tong, X. L. Li, Y. H. Duan, and C. P. Yu, "Direct numerical simulation of supersonic turbulent boundary layer subjected to a curved compression ramp," Phys. Fluids **29**, 125101 (2017).
[26]F. L. Tong, C. P. Yu, Z. G. Tang, and X. L. Li, "Numerical studies of shock wave interactions with a supersonic turbulent boundary layer in compression corner: Turning angle effects," Comput. Fluids **149**, 56–69 (2017).
[27]M. Wu and M. P. Martin, "Direct numerical simulation of supersonic turbulent boundary layer over a compression ramp," AIAA J. **45**(4), 879–889 (2007).
[28]M. P. Martin, E. M. Taylor, M. Wu, and V. G. Weirs, "A bandwidth-optimized WENO scheme for the effective direction numerical simulation of compressible turbulence," J. Comput. Phys. **220**, 270–289 (2006).
[29]G. Jiang and C. Shu, "Efficient implementation of weighted ENO schemes," J. Comput. Phys. **126**(1), 202–228 (1996).
[30]S. Gottlieb and C. W. Shu, "Total variation diminishing Runge–Kutta Schemes," Math. Comput. **67**, 73–85 (1998).
[31]F. L. Tong, X. X. Yuan, J. Lai, J. Y. Duan, D. Sun, and S. W. Dong, "Wall heat flux in a supersonic shock wave/turbulent boundary layer interaction," Phys. Fluids **34**, 065104 (2022).
[32]S. Pirozzoli, F. Grasso, and T. B. Gatski, "Direct numerical simulation and analysis of a spatially evolving supersonic turbulent boundary layer at $M = 2.25$," Phys. Fluids **16**, 530 (2004).
[33]J. Fang, A. A. Zheltovodov, Y. F. Yao, C. Moulinec, and D. R. Emerson, "On the turbulence amplification in shock-wave/turbulent boundary layer interaction," J. Fluid Mech. **897**, A32 (2020).
[34]M. B. Sun, N. D. Sandham, and Z. W. Hu, "Turbulence structures and statistics of a supersonic turbulent boundary layer subjected to concave surface curvature," J. Fluid Mech. **865**, 60–99 (2019).
[35]Q. C. Wang, Z. G. Wang, M. B. Sun, R. Yang, Y. X. Zhao, and Z. W. Hu, "The amplification of large-scale motion in a supersonic concave turbulent boundary layer and its impact on the mean and statistical properties," J. Fluid Mech. **863**, 454–493 (2019).
[36]Y. S. Zhang, W. T. Bi, F. Hussain, and Z. S. She, "A generalized Reynolds analogy for compressible wall-bounded turbulent flows," J. Fluid Mech. **739**, 392–420 (2014).
[37]L. P. Erm and P. N. Joubert, "Low Reynolds number turbulent boundary layers," J. Fluid Mech. **230**, 1–44 (1991).
[38]S. Pirozzoli, M. Bernardini, and F. Grasso, "Direct numerical simulation of transonic shock/boundary layer interaction under conditions of incipient separation," J. Fluid Mech. **657**, 361–393 (2010).
[39]J. L. Lumley, "Computational modeling of turbulent flows," Adv. Appl. Mech. **18**, 123–176 (1978).
[40]V. Pasquariello, M. Grilli, S. Hickel, and N. A. Adams, "Large-eddy simulation of passive shock-wave/boundary-layer interaction control," Int. J. Heat Fluid Flow **49**, 116–127 (2014).
[41]B. Nottebrock, K. J. Genurts, and W. Schröder, "Wall-shear stress measurements in an adverse pressure gradient turbulent boundary layer," AIAA Paper No. 2012-2978, 2012.
[42]S. Grosse and W. Schröder, "Wall-shear stress patterns of coherent structures in turbulent duct flow," J. Fluid Mech. **633**, 147–158 (2009).
[43]K. R. Sreenivasan and R. A. Antonia, "Properties of wall shear stress fluctuations in a turbulent duct flow," Trans. ASME E: J. Appl. Mech. **44**, 389–395 (1977).
[44]C. D. Daniel, S. Laizet, and J. C. Vassilico, "Wall shear stress fluctuations: Mixed scaling and their effects on velocity fluctuations in a turbulent boundary layer," Phys. Fluids **29**, 055102 (2017).
[45]L. Duan, M. M. Choudhari, and M. W. Wu, "Numerical study of acoustic radiation due to a supersonic turbulent boundary layer," J. Fluid Mech. **746**, 165–192 (2014).
[46]S. Jeon, H. Choi, J. Y. Yoo, and P. Moin, "Space-time characteristics of the wall shear-stress fluctuations in a low-Reynolds-number channel flow," Phys. Fluids **11**, 3084 (1999).
[47]M. Bernardini and S. Pirozzoli, "Wall pressure fluctuations beneath supersonic turbulent boundary layers," Phys. Fluids **23**, 085102 (2011).
[48]B. Guerrero, M. F. Lamber, and R. C. Chin, "Extreme wall shear stress events in turbulent pipe flows: Spatial characteristics of coherent motions," J. Fluid Mech. **904**, A18 (2020).
[49]C. Pan and Y. Kwon, "Extremely high wall-shear stress events in a turbulent boundary layer," J. Phys.: Conf. Ser. **1001**, 012004 (2018).
[50]J. Jeong and F. Hussain, "On the identification of a vortex," J. Fluid Mech. **285**, 69–94 (1995).
[51]J. H. Lee and H. J. Sung, "Very-large-scale motions in a turbulent boundary layer," J. Fluid Mech. **673**, 80–120 (2011).
[52]R. J. Adrian, C. D. Meinhart, and C. D. Tomkins, "Vortex organization in the outer region of the turbulent boundary layer," J. Fluid Mech. **422**, 1–54 (2000).
[53]J. I. Cardesa, J. P. Monty, J. Soria, and M. S. Chong, "The structure and dynamics of backflow in turbulent channels," J. Fluid Mech. **880**, R3 (2019).
[54]M. Bross, T. Fuchs, and C. Kähler, "Interaction of coherent flow structures in adverse pressure gradient turbulent boundary layers," J. Fluid Mech. **873**, 287–321 (2019).
[55]D. Sun, Q. L. Guo, X. X. Yuan, H. Y. Zhang, and C. Li, "A decomposition formula for the wall heat flux of a compressible boundary layer," Adv. Aerodyn. **3**, 33 (2021).
[56]C. Cheng, W.-P. Li, A. Lozano-Durán, and H. Liu, "Identity of attached eddies in turbulent channel flows with bidimensional empirical mode decomposition," J. Fluid Mech. **870**, 1037–1071 (2019).

Downloaded from http://pubs.aip.org/aip/pof/article-pdf/doi/10.1063/5.0113514/16584511/105109_1_online.pdf

Published under an exclusive license by AIP Publishing